THE PENNSYLVANIA STATE UNIVERSITY
SCHREYER HONORS COLLEGE

DEPARTMENT OF BIOMEDICAL ENGINEERING

COMPARING NOVEL TECHNIQUES FOR MEASURING THE BENDING MODULUS OF LIPID BILAYER MEMBRANES IN ERYTHROCYTES

NICHOLAS FRAZZETTE
SPRING 2016

A thesis
submitted in partial fulfillment
of the requirements
for a baccalaureate degree
in Bioengineering
with honors in Bioengineering

Reviewed and approved* by the following:

Peter J. Butler
Professor of Biomedical Engineering
Thesis Supervisor

William O. Hancock
Professor of Biomedical Engineering
Honors Adviser

* Signatures are on file in the Schreyer Honors College.

ABSTRACT

Cellular mechanobiology is the area of biology in which mechanical forces are sensed by cells, and transduced into intracellular biochemical signals, leading to changes in cell function. Cells interact with their environments principally through the cell membrane, where lipids, proteins, and other receptors transmit mechanical and chemical signals to the cell interior. More recently, research has shown that as the lipid bilayer membrane bends or stretches, protein activation can occur as areal changes can induce protein conformational changes or changes in protein clustering. Critically, therefore, understanding the energies and forces that determine membrane bending will help understand the nature of mechanotransduction and its associated cell signaling. The erythrocyte membrane is a popular model membrane of study due to the known flexibility of erythrocytes as they flow through the vasculature. In this thesis, a novel method is presented of determining membrane bending modulus and area-per-lipid using lifetime fluctuations of embedded fluorophores. As the membrane bends and flexes, the area around individual lipids or fluorescent lipid analogs is reduced or expanded due to compression or tension, respectively. Because the fluorescence lifetime of many fluorophores is strongly regulated by the immediate local environment of the fluorophore, these areal changes lead to detectable lifetime changes. Using this method, it is shown that the bending modulus of healthy erythrocytes is approximately 55.60 k_BT, in good agreement with commonly obtained literature values, and the area per lipid is approximately 44.22 $Å^2$, a previously unreported value because it is inaccessible with currently available techniques. These values were also experimentally validated against a novel, low power optical trapping method for detecting membrane mechanics. Importantly, the use of fluorescence lifetime fluctuations represents a simple and versatile technique that can be applied to many cell solution states, such as varying pH or osmolarity, as well as many different types of cells.

TABLE OF CONTENTS

LIST OF FIGURES

LIST OF TABLES

ACKNOWLEDGEMENTS

First and foremost, I am deeply thankful to Dr. Peter Butler, my thesis advisor and research mentor. His constant support over 4.5 years of biomedical engineering research has instilled me in an ability to question and think critically, problem solve in the face of challenges, and appreciate scientific discovery. His advice and mentorship proved to be the foundation for this work, and I am sure the skills learned in his lab will serve me well throughout my entire career.

I also thank Dr. William Hancock and Herbert Lipowsky for their service on my thesis committee. Their expertise in the fields of mechanobiology, erythrocyte dynamics, and experimental design and analysis proved invaluable to the final draft of this work.

The other members of Dr. Butler's Mechanobiology Lab, in particular Seoyoung Son and Pansy Leung, have given me incredible advice, support, and training on many of the methods and techniques that made this work possible. Additionally, their constant feedback in meetings prompted many of the questions and conclusions presented here.

Finally, I am thankful to my family, and in particular my parents, for always encouraging an air of curiosity and investigation and a passion for construction and design. I would not be the engineer I am today without their support.

Chapter 1 – Introduction to Time-Correlated Single-Photon Counting and Optical Trapping

Time-correlated single-photon counting (TCSPC) is uniquely well-suited to investigating the mechanics of cell membranes. This thesis demonstrates how TCSPC can be used to determine the changes in the fluorescent parameters, particularly in fluorescence lifetime, reveal changes in the relative stiffness of a cell membrane, expressed as a bending modulus of that membrane. Lipophilic fluorophores, such as 1'-dioctadecyl-3,3,3'3'-tetramethylindocarbocyanine perchlorate (DiI), can be embedded in the membranes of living cells and are responsive to changes in free-area-per-lipid, a membrane parameter that is correlated with membrane bending modulus[1]. Whereas previous methods of lipid membrane analysis require a synthetically produced membrane[2–6] or a computational model[7], there are much fewer methods for analyzing live, naturally produced cells such as human-derived erythrocytes.

One additional method aside from TCSPC is to use a low-power optical trap (LPOT) setup to directly measure membrane fluctuations as they deflect a laser beam[8]. These fluctuations in laser intensity are converted to distance fluctuations, and are plotted as power spectral density function that is fit to a characteristic equation derived from Helfrich membrane theory. This theory has also been applied to living human erythrocytes to investigate the ATP dependence and spectrin network dependence of erythrocyte membranes mechanics[9]. In addition to demonstrating the use of TCSPC as a measurement of membrane bending modulus, this thesis will also compare both the LPOT and TCSPC methods as two of the most recently developed methods for living cell membrane analysis. Comparison of these techniques is warranted by the fact that LPOT directly measures membrane height fluctuations from a mean, which is the parameter specifically modeled in Helfrich theory. Furthermore, LPOT detects these fluctuations in an area of the membrane close to the size of a laser spot used in TCPSC. Importantly, however, TCSPC-based analysis looks at area-per-lipid changes with changes in membrane bending and requires an

additional derivation of area change as a function of membrane height from a neutral plane. Therefore, LPOT is considered a standard that is used here to validate the new TCSPC- based technique.

Briefly, this chapter focuses on the basic principles of TCSPC and fluorescence. Then, the basic principles of optical trapping are introduced.

Section 1.1 Principles of Fluorescence

Luminescence is, generally, the emission of electromagnetic energy ranging from the ultraviolet to the infrared wavelengths. Broadly speaking, luminescence as it related to light interacting with matter, "photoluminescence", can be broken down into fluorescence, of principle interest in this work, and phosphorescence, a much slower process. Luminescence as a property is characteristic of a variety of organic and inorganic molecules. In phosphorescence, an electron is excited to a higher energy state, but instead of de-exciting down the same pathway, it undergoes intersystem crossing such that its electron spin matches that of its electron pair. This is traditionally considered a forbidden state in quantum mechanics, and thus causes a very slow decay process (on the order of minutes).

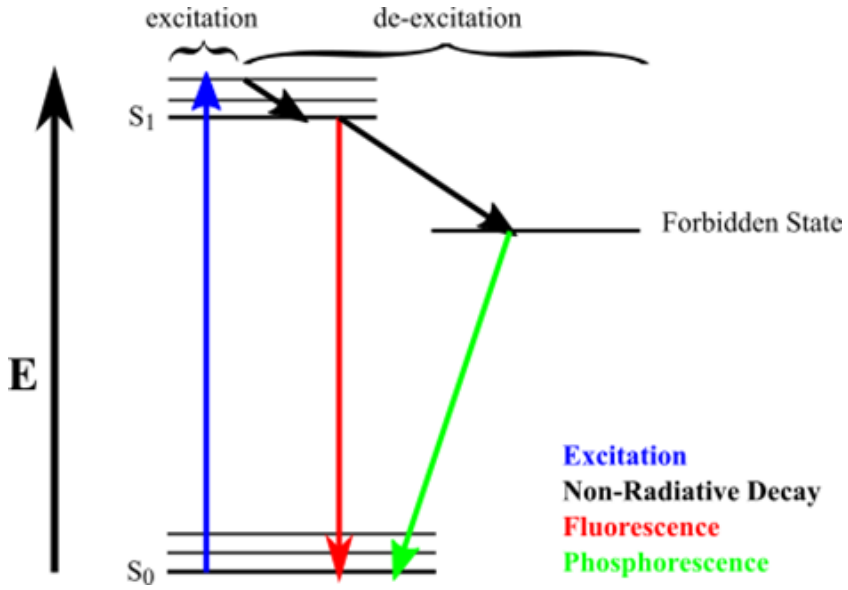

Figure 1.1 Jablonski diagram demonstrating energy transitions of excitation, fluorescence, and phosphorescence

Fluorescence, on the other hand, is a much more rapid process (on the order of nanoseconds). In fluorescence, a molecule absorbs an incident photon to excite an electron to a higher energy state, identical to phosphorescence. However, the de-excitation pathway is significantly different. Following very low-energy, non-radiative energy decay, from processes such as molecular vibration, the principle amount of absorbed energy is then re-emitted in the form of another photon. This emitted photon is, in almost all cases, at a longer wavelength than the absorbed photon because of the energy lost to non-radiative decay processes. An example schematic diagram, called a Jablonski plot, is provided in figure 1.1.

An excellent reference on the principles of molecular fluorescence is Valeur[10].

Section 1.2 Time-Correlated Single Photon Counting

There are several modern microscopy techniques that all rely on fluorescence, which allow for much higher resolution than typical bright-field microscopy. Time-correlated single photon counting (TCSPC) is one such advanced technique.

TCSPC is a time-resolved fluorescent technique capable of discerning the nanosecond fluorescent lifetimes of common fluorophores; additionally, it is capable of discerning these fluorophores singularly[11]. Using a picosecond pulsed laser, the precise times of the emitted fluorescent photon can be logged using a specialized PCI card and software. These times can be analyzed to retrieve important data from the fluorophore.

The picosecond pulsed laser emits a beam at 80 MHz, producing a pulse every 12.5 ns, which is split into an excitation pulse and a sync pulse. The excitation pulse is expanded from a fiber optic cable and filtered to a precise wavelength, then refocused through an objective into the sample. The sample then emits photons in all directions; some of these photons are recollected by the objective and filtered and

focused down into a confocal pinhole entrance to a fiber optic cable. The signal is then amplified in a photomultiplier tube (PMT) and run through a detector control card (DCC). The DCC is a maximum threshold card that automatically turns off the PMT if the intensity is too high, to protect the photodetector in the PMT[12]. This setup is diagramed in figure 1.2; the colors of each beam demonstrate the shift in wavelength due to fluorescence.

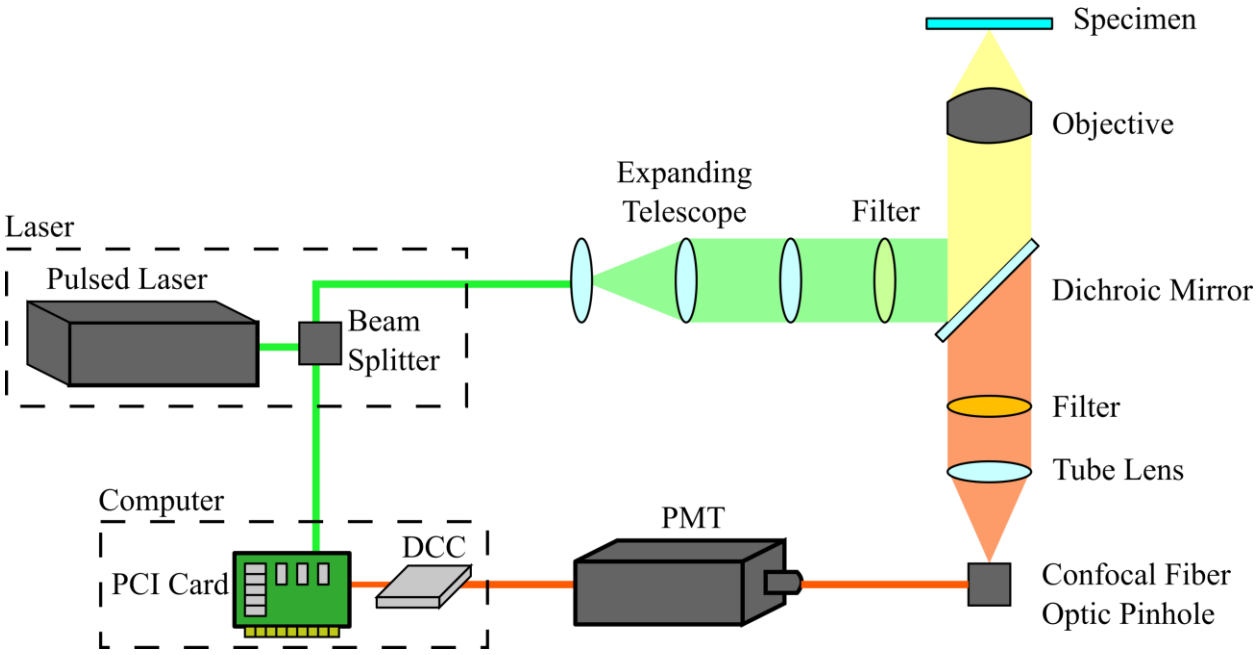

Figure 1.2. TCSPC Example Setup

Generally, shifts in fluorescence range in the tens of nanometers. Importantly, a typical TCSPC setup uses an optical arrangement identical to confocal microscopy; however, the data recovered is not a visual image of the specimen but rather a series of logging times of the arrival of sync and emission photons. These times are used to calculate macrotimes, the time between a

particular emission and the start of the experiment, and microtimes, the time between a particular excitation photon and emission photon. Generally, microtimes are relatively similar to each other and distributed according to Poisson statistics around a mean. Macrotimes, however, continue to increase as the data collection time increases. These two measurements are schematically represented in figure 1.3.

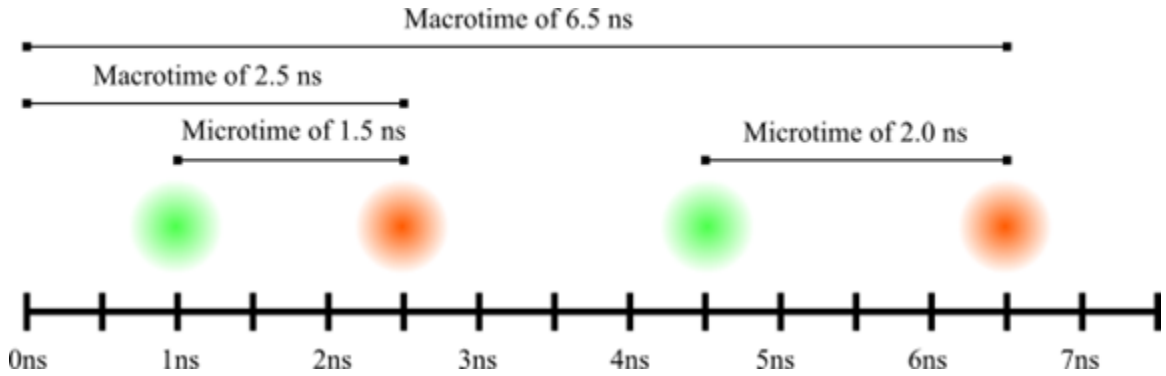

Figure 1.3. Schematic of macrotime and microtime

The most intuitive measurement technique to record the microtimes of each photon would be to start timing upon each received sync pulse from the laser, and stop on the following emission pulse. However, due to the extremely low fluorophore concentrations required by TCSPC and the fact that not every excitation event leads to emission that ultimately reaches the PMT, triggering data capture based on collection of emitted photons could be extremely inefficient. In addition, the nature of determining the microtime is through a time-to-amplitude converter (TAC) in which a trigger starts a voltage ramp that is stopped by another pulse. If the system were to trigger the TAC on every excitation pulse, there may be many instances where the ramp would not be stopped. One alternative is to include an automated script to turn off the recording after a certain time threshold; however, this solution will require heavy and rapid computation, and could still potentially limit the collection of data depending on the length of the threshold. A more reliable and less computationally intensive technique is called the reverse start-stop technique[13]. Using this method, timing with the TAC only "begins" with the arrival of an emission photon and is stopped with the sync pulse from the laser. If the sync pulses are kept perfectly regular, the appropriate start time can be back-calculated by moving back to the nearest sync pulse relative to the particular emission photon. The only major limitation for using this method is that the fluorophore chosen must have a lifetime shorter than the pulse width of the laser; however, there are myriad fluorophores with sub-10ns lifetimes, meaning that a 100MHz laser easily fulfills this criterion and will still collect data quickly.

In addition to collecting the photons, a number of electrical components convert the photon signal into an electronic impulse[12]. First, a constant fraction discriminator (CFD) processes the data. The CFD is a basic threshold that limits the amount of noise from background light, which can trigger the detector. The CFD also ensures that the amplitude of the light signal does not affect the electronic signal, since only the time information is desired. In order to accomplish this, the CFD duplicates, delays, and inverts an incoming photon pulse. Then, the original and inverted-delayed pulse are summed to yield a new curve which necessarily crosses the zero regardless of the amplitude of the original pulse; it is at this zeroing cross that a signal is output from the CFD. The next component is a time-to-amplitude converter (TAC). The TAC is a voltage ramp generator that produces an electrical signal from a start and stop pulse, the sync and emission photon respectively. Using the above justification for a reverse start-stop triggering, the TAC can generate meaningful electronic data directly related to each incoming photon pair time-difference. Finally, an analog-to-digital convert (ADC) digitizes the data for logging into histograms.

Section 1.3 Fluorescence Correlation Spectroscopy

Fluorescence Correlation Spectroscopy (FCS) is a powerful data analysis technique that provides information on particle size and diffusion of fluorophores from information collected via TCSPC[11,14–16]. In particular, it is very efficient at assessing the diameters of sub-200nm particles at extremely low (on the order of 1 nM) concentrations[11]. FCS relies on the use of confocal optics to create a femtoliter Gaussian laser volume that is capable of probing nanometer-ranged particles for fluctuations in their fluorescence. These fluctuations are then autocorrelated to provide characteristic diffusion times. As a particular fluorophore diffuses first into focused Gaussian laser spot, and the emitted photons through the confocal pinhole, the fluorescence fluctuates around some mean value $\langle F \rangle$ (figure 1.4). These fluctuations in fluorescence intensity can be autocorrelated according to the function[11]:

$$G(\tau) = \frac{\langle \delta F(t+\tau)\delta F(t)\rangle}{\langle F(t)\rangle^2} \quad \textbf{(1)}$$

where time (t) and lag time (τ) vary across all times in the sample. The particular time (t) is the macrotime according to the section above, and lag time (τ) varies from zero to the maximum macrotime.

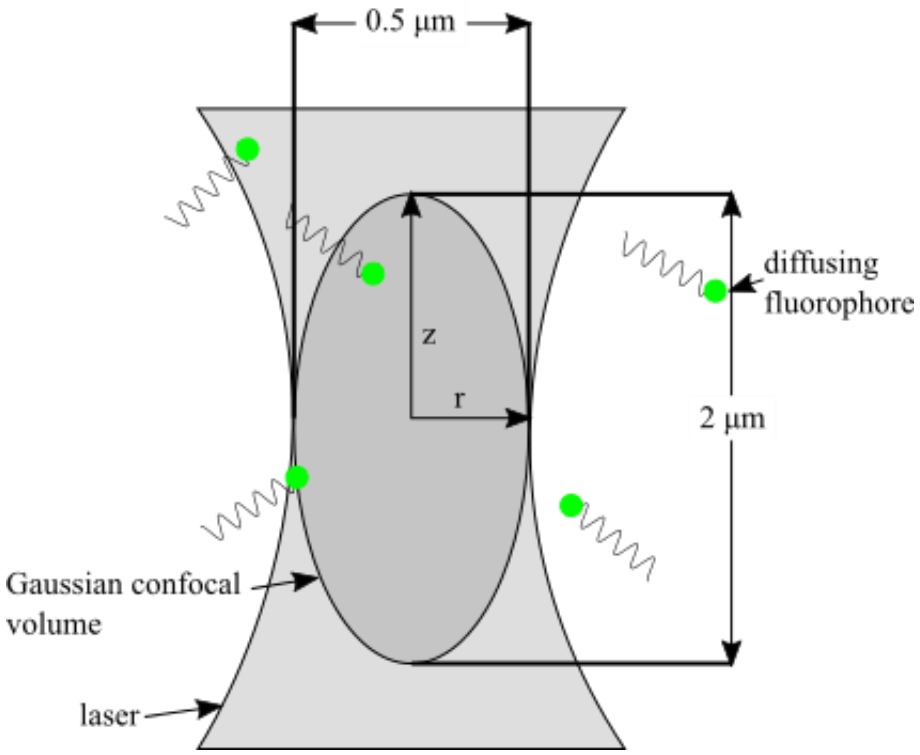

Figure 1.4 Gaussian confocal laser volume with diffusing particles

Several literature sources can provide the appropriate fitting functions for these autocorrelation curves. In particular, to fit a 3D, single species diffusion, the following equation[14,15] is used:

$$G(\tau) = \frac{1}{N}\left[\frac{1}{1+\frac{\tau}{\tau_D}}\right]\left[\frac{1}{1+\left(\frac{1}{\omega}\right)^2\left(\frac{\tau}{\tau_D}\right)}\right]^{1/2} \quad \textbf{(2)}$$

where N is the average number of particles in the Gaussian volume, t_D is the characteristic diffusion time, and ω is the structure factor of the volume defined as the ratio z/r. Often, with a sufficiently small confocal volume and low concentration of fluorophores, N will be on the order of 1 and not more than 10;

these are ideal measurement parameters. In order to translate the characteristic diffusion time to particle radius, the diffusion coefficient of the particle must be determined according to equation:

$$r^2 = 4D\tau_D \quad \textbf{(3)}$$

where *r* is the radius of the confocal volume. Inherently, this equation has two unknowns, *r* and *D*, after curving fitting data from the autocorrelation curve. In order to make this equation solvable, a calibration must be conducted with a particle of known diffusion coefficient *D*. For certain molecular fluorophores, these data are literature-derived. Commonly used polymeric spheres can also be used, whose radius *R* can easily be converted into a diffusion coefficient, *D*, according to equation:

$$D = \frac{k_b T}{6\pi\eta R} \quad \textbf{(4)}$$

where k_B is the Boltzmann constant, *T* is the absolute temperature, and η is the solvent viscosity. If the excitation laser is stable and is not adjusted between calibration and sample measurement, it can be assumed that the diffusion distance r^2 does not significantly change between both samples. Combining equations **(3)** and **(4)** can give a relation between this distance, the diffusion time recovered by the autocorrelation, and the unknown radius of the particle, shown in equation:

$$R(r^2, \tau_D) = \frac{k_b T}{6\pi\eta\left(\frac{r^2}{4\tau_D}\right)} \quad \textbf{(5)}$$

There are several other autocorrelation fitting functions that can be used to determine the characteristic diffusion time in order to account for different parameters; FCS is not limited to these specific parameters. Other commonly used functions can analyze multiple species[14,16–18] (particles of different radii), particles in a triplet state[14,19], and other phenomena or conditions[20]. An example autocorrelation curve and fit are provided in figure 1.5 (*k* is analogous to ω and C is a fitting parameter that accounts for the occurrence when the autocorrelation does not decay to 0.)

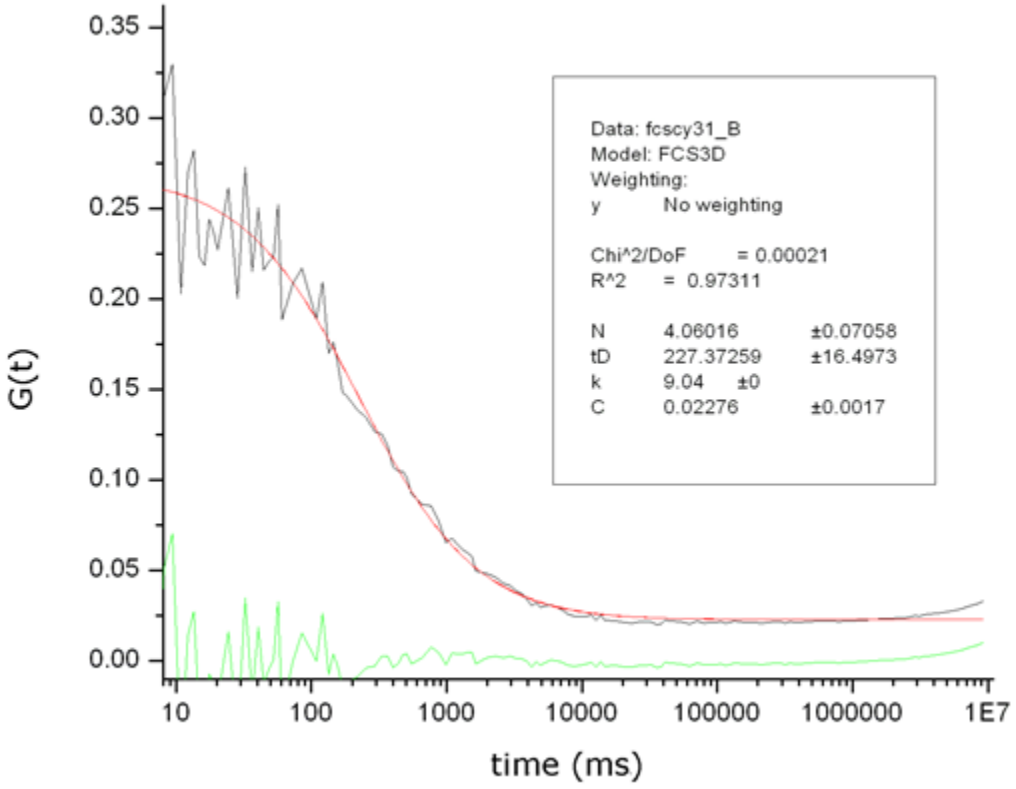

Figure 1.5 Example FCS curve and fit

Section 1.4 Fluorescence Lifetime Spectroscopy

Fluorescence Lifetime Spectroscopy is another powerful analysis tool based on the data collected from TCSPC that can reveal subtle changes in the photophysics of fluorophores. Fluorescence lifetime, τ, is the finite duration of time during which an electron remains in the excited state. As discussed previously, there are two methods of energy decay from this excited state, radiative and non-radiative; as such, there are two decay rates which control the magnitude of the lifetime:

$$\tau = \frac{1}{k_r + k_{nr}} \quad \textbf{(6)}$$

Because lifetime of fluorophores used in TCSPC often range on the order of 1 ns, a rapidly pulsed laser (on the order of 80MHz) must be used to provide a large enough window to observe the full fluorescence lifetime plus the instrument response function, but also collect data rapidly enough that a meaningful result can be obtained. Then, fitting the data into equation **(7)** can provide the lifetime:

$$I(t) = \sum_i \alpha_i e^{-t/\tau_i} \quad \textbf{(7)}$$

In equation **(7)**, *I(t)* is the observed fluorescence decay, α_i the fraction of fluorescing molecules (normalized to unity) and τ_i is the lifetime of the fluorescing molecules. While fluorescence only operates on first order kinetics[21], often times *i* is set to a second order decay which provides better fits and more accurate data[22–24]. The two recovered lifetimes are averaged according to their intensity. However, this method ignores a critical errors characteristic of real measurements. The instrument response function (IRF) is a systematic error based on the detector shot noise and electronic noise during analog to digital conversion. Ordinarily such processing times are negligible when processing data; however, because fluorescence operates on the nanosecond scale, these errors become significant. By observing the "fluorescence" of a totally quenched sample, the IRF can be obtained. It can be assumed that the observed decay *I(t)* is some convolution of the IRF and the true fluorescence decay[21]. The decay function can be modified to account for the IRF; one example of such a modified function is shown in equation:

$$I(t) = IRF * J(t) = IRF * \sum_i \alpha_i e^{-t/\tau_i} \quad \textbf{(8)}$$

where *J(t)* is the true fluorescence decay and "*" is the convolution operator. There are several methods for obtaining the true decay from the observed decay. Most commonly, the IRF and true decay are iteratively reconvoluted with varying parameters for the true decay until the resulting equation matches the observed decay using a least squares method of analysis. Those parameters which provided the best fit can then be exported. Commonly, the data collected is sorted into a histogram with an exponential distribution, and the convolution is fit to the shape of this histogram. An example reconvolution is shown

in figure 1.6; residuals and X^2 are used to determine goodness of fit. Other methods of recovering lifetime data including using moments analysis. Fluorescence lifetime follows a Poisson distribution. A useful feature of this distribution is that the first moments, or means, of convoluted samples sum. Therefore, if the first moment of an IRF is subtracted from the first moment of a collection of microtimes convoluted with that IRF, the remaining value will be the average of those microtimes alone. Conveniently, for an exponential decay such as fluorescence, the first moment or mean also represents the time constant, or in this case, the fluorescence lifetime[25].

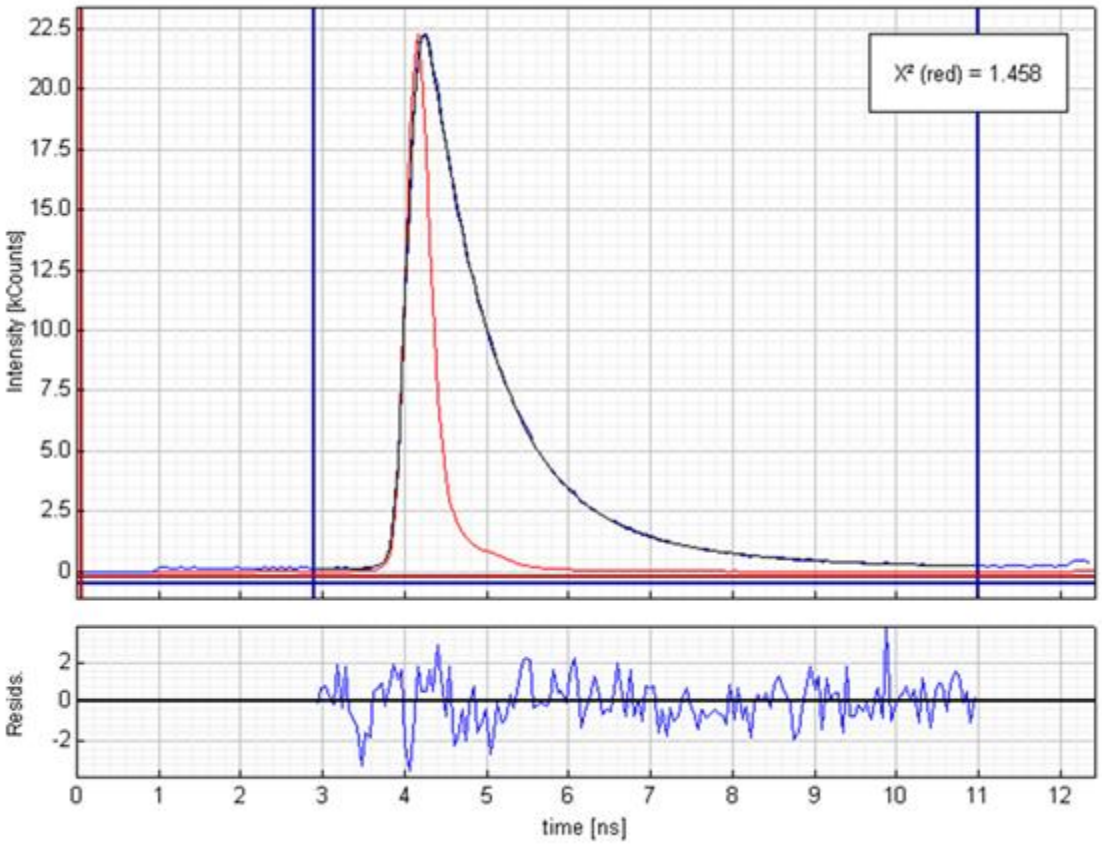

Figure 1.6 Example lifetime curve and fit

Radiative decay is largely independent of external influences from the solvent or neighboring molecules. However, non-radiative decay of certain fluorophores[26,27] can be strongly influenced by the local environment due to steric hindrance or ionic charge. For example, binding a fluorophore to a larger particle prevents a certain degree of vibrational or rotational energy dissipation; incorporating into a

particle or lipid membrane will further reduce vibrational or rotational degrees of freedom or prevent isomerization. Small but detectable changes in fluorescence lifetime can therefore suggest changes in the local environment of fluorophores.

Section 1.5 Optical Trapping

Optical traps, sometimes called optical tweezers, are a powerful and novel technique for measuring a variety of biological phenomena. In their general form, optical traps focus a laser down on semitranslucent micron sized particles to trap them in place, not unlike a micro-scale "tractor beam". According to Snell's law **(9)**, the angle of the light path from the laser is bent upon transitioning from the sample medium, such as water or air, into the sample itself, such as a tracer particle or cell.

$$\frac{\sin\theta_1}{\sin\theta_2} = \frac{n_2}{n_1} \qquad \textbf{(9)}$$

As light refracts across the interface, individual photon paths shift according to the angle they strike the particle. Photons which strike directly on the particle at 0° relative to the normal will not refract; all other photons will be refracted towards the normal, as most particles have higher indices of refraction than the surrounding water. Critically, however, photons on either side of the particle will be refracted equally but opposite, as shown in figure 1.7.

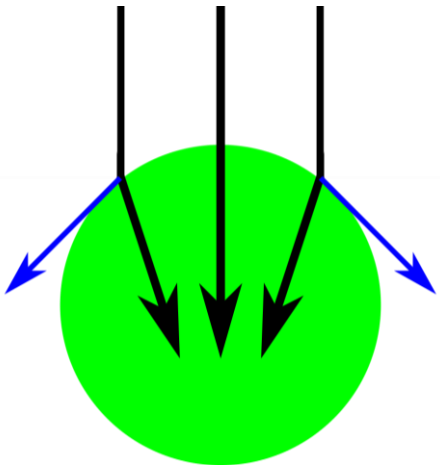

Figure 1.7 Optical Trap force diagram

Because photons possess momentum, changes in their direction must be accompanied by a corresponding force, in order to account for the momentum change. As mentioned above, these force changes will be equal and opposite for photons equal distances from the center of the particle. However, due to the curvature of the particle, the forces will not be totally along the horizontal (as shown in figure 1.7). If the particle rests exactly in the middle of a Gaussian laser profile in the xy-plane, these forces will be equal and opposite. However, as the particle moves either left or right, the intensities will shift, causing one force to be greater than the other and accelerating the particle back towards the center. If the laser also has a Gaussian z-profile, the particle will also be accelerated to the center of the laser intensity on the z-axis. Critically, the laser must be operated at a high power to affect a great enough trapping force. Neuman and Block provide a comprehensive review of optical trapping[28]. This experimental setup can also be used for an interferometric technique for detecting the fluctuations of lipid membranes, as recently described by Betz and Sykes[8,9]. Adjustments required for this setup will be discussed later.

Chapter 2 – The Erythrocyte Membrane

Lipid bilayer membranes surround all types of cells and provide both a barrier from extracellular elements and one of the key methods for a cell's communication and interaction with its extracellular environment. The widely accepted model today is an improvement on the fluid mosaic model. Lipids are believed to show some organization into rafts that incorporate certain proteins, facilitating or directing the movement of surface proteins. This chapter will serve as an introduction to the structure of membranes, to the importance of their mechanical parameters, and to the commonly used Helfrich model to describe membrane bending.

Section 2.1 Membranes are Flexible Lipid Bilayers

The cell membrane is the principle barrier between almost all mammalian cells and their environments. It is a fluid, flexible membrane made of amphiphilic lipids, the most common among which are phospholipids. Embedded in these lipids are (1) proteins that play significant roles in cell signaling (e.g. receptors) and function (e.g. ion channels), as well as tissue structure (e.g. junctions) and (2) cholesterols that play an important role in regulating lipid bilayer fluidity. Lipids are a class of biomacromolecule with a hydrophilic head group and hydrophobic tails, which leads to their amphiphilic nature. This nature also contributes to their ability to form into superstructures such as micelles and bilayer membranes. Lipids organize to minimize hydrophobic-hydrophilic interaction between water (the primary component of both intracellular and extracellular fluids) and alkyl chain tails. While organized into lipid bilayers, individual lipid molecules continue to demonstrate a significant degree of mobility and flexibility. In addition to their mobility, lipids are believed to influence the behavior of other membrane elements, such as proteins, through their organization in lipid rafts[29–31].

Lipid mobility is partly a factor of lipid free volume V_f, or the volume between lipid molecules. If lipids are approximated as rigid rods, volume per lipid, $V_{o,}$ can be broken down into two components: the

roughly circular head group area A_o and lipid length L defined by the alkyl chain length (figure 2.1). After DiI staining, the fluorescent lipid analog sits slightly lower in the membrane, such that the distance d is less than half the membrane thickness. The total volume per lipid is equal to the free volume plus this lipid volume. Lipid mobility is partly due to alkyl chain length; shorter chains have fewer sites for hydrophobic interactions and therefore are more fluid.

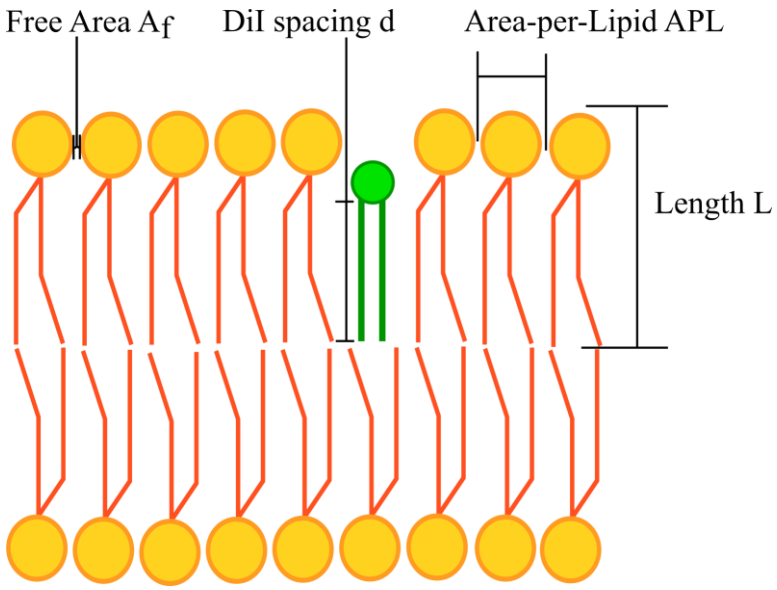

Figure 2.1 Unstressed lipid bilayer

Lipid mobility is related to membrane flexibility, or the ability of the membrane to bend along some defined curvature. As membranes bend, the free area-per-lipid increases or decreases based on the concavity of a particular leaflet of the membrane (figure 2.2). Steric hindrance of tail groups or head groups prevents bending without modulating free area, and hydrophobic interactions between chains limit how wide the "wedges" between individual lipids can open. Both of these limit the curvature of enclosed vesicles to minimum diameters of approximately 25 nm; conversely, vesicles as large as 1 mm have been generated synthetically. Additionally, these forces create a resistance to lateral tension in the membrane. Membrane bending and tension, in addition to direct interaction with lipids, all have potential to affect protein function. Alberts provides an excellent reference on lipid bilayer structure and properties[32].

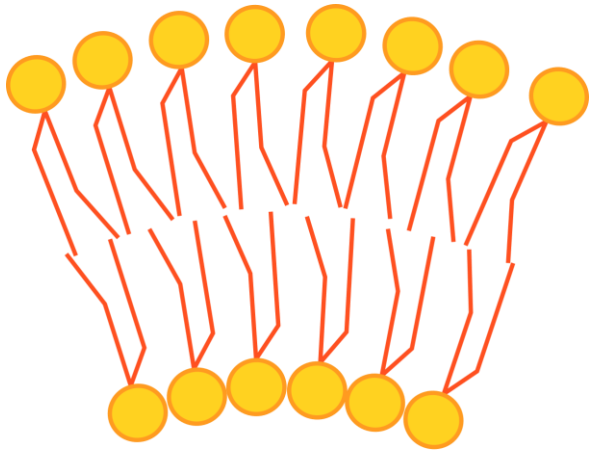

Figure 2.2 Stressed lipid bilayer

The erythrocyte membrane, in particular even among other eukaryotic cell membranes, contains an additional membrane component that plays a large role in membrane mechanics. Most eukaryotic cells contain a three-dimensional cytoskeleton composed of three classes of filaments that provide a semirigid structure to the cell. Erythrocytes, on the other hand, contain a two-dimensional network of spectrin which sits immediately beneath the membrane, as shown in figure 2.3. This spectrin network is composed of a roughly triangular mesh of tetramers of α/β spectrin (blue and red) with side length 46 nm where each node of the network (purple) serves as a connection point to the membrane through protein junctions (light green); other membrane connections directly to a spectrin side are also possible (magenta)[33,34]. Additionally, the red blood cell membrane in particular is heavily saturated with proteins, up to 50% by weight, and carbohydrates, up to 15%. Of the remaining space occupied by lipids, another approximately 50% by mole are cholesterol while the final 50% are traditional phospholipids[34]. Taken into account, this leads to an observed membrane thickness of 4 nm[35]. All of these membrane components make the erythrocyte membrane unique among cell membranes.

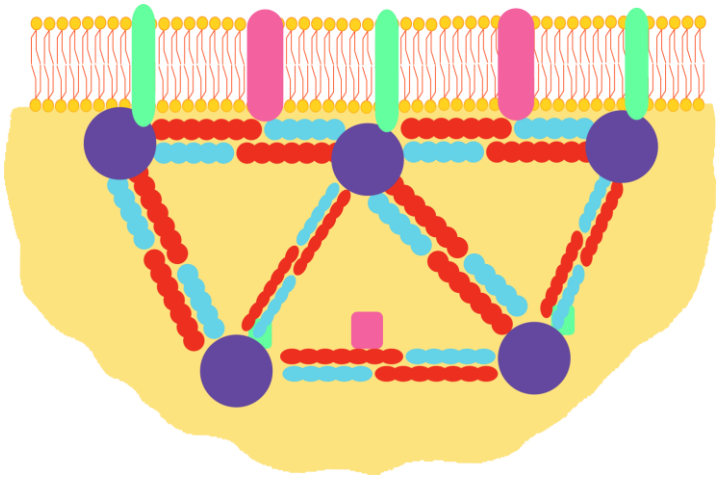

Figure 2.3 Erythrocyte membrane with spectrin network

Section 2.2 Membranes are Force Sensors

While there is a significant amount of research to support the importance of cell-embedded proteins and receptors in cell communication and interaction, a growing body of research also implicates the mechanical properties of the membrane itself in such functions. Cells exhibit a significant receptivity to mechanical forces, or the ability to sense mechanical forces and convert them into biological signals[36–38]. Membrane bound proteins, even in the absence of common lipids, exhibit a mechanical sensitivity; on the other hand, the activity of some mechanical sensitive channels show an intimate linkage to nearby lipids[39]. Additionally, cell membrane mechanics are believed to influence cellular uptake of small particles, such as fluorescent tracers with potential extrapolation to drugs or viruses[40]. In fact, cellular membrane mechanics have even been implicated in maintaining health, or, in instances of mechanics gone awry, in causing disease[41].

Of critical importance is the nature of proteins in the erythrocyte membrane as it relates to force sensitivity. Proteins can by activated through conformational changes or spatial changes relative to other proteins or other lipids. Both activities can be affected by non-specific interaction with lipids whereby the mechanical properties of the membrane influence protein behavior by changing the local environment of

the protein. For example, significant energy is saved by matching hydrophobic thickness of embedded membrane proteins to the hydrophobic thickness of the lipid bilayer, and mismatching can induce conformational changes in the protein[42,43]. Bending of the membrane or shear stress along it may open transient invaginations which can expose the hydrophobic core of the protein to water and induce a conformational change[44]. Membrane bending may also influence the construction or dissolution of lipid rafts, which can alter protein behavior by, for example, changing the kinetics of receptor ligand interactions[45].

Fluidity of the membrane and applied lateral tension can affect lipid diffusion[46,47] and the organization of lipid rafts[48] can also alter behavior as mentioned before. In all these examples, understanding the mechanical parameters of the membrane's ability to bend and stretch can reveal the nature of certain cells to react to certain mechanical forces. However, membrane bending is significantly less energetically costly than membrane stretching[44], suggesting that bending could be a significant source of membrane protein activation[49].

Not only can membrane bending itself modulate protein activity, but it can also passively allow for the movement and organization of proteins in the cell membrane. Particularly in erythrocytes, the underlying spectrin cytoskeleton can potentially serve as a corral for embedded proteins. As the membrane bends and fluctuates away from this network, proteins may have enough space to jump from one corral to the next or hitch themselves along a certain spectrin fiber[50]. This corralling represents another method by which certain proteins are brought into proximity with each other.

While bending in the cell membrane occurs on a wide range of modes, in these scenarios described above, only bending that occurs on the small modes will have an appreciable impact on protein activation. Large waves of membrane bending will result in a shared stretch per lipid or per protein may not cause great enough an invagination to warrant conformational change or a diminished height change away from the underlying spectrin network to provide enough space for proteins to diffuse. Small bending modes, therefore, have the potential for greater impact on mechanotransduction in cells.

Section 2.3 Introduction to Helfrich Membrane Theory

Many three-dimensional enclosed volumes in nature exhibit spherical shapes as their lowest energy conformations, particularly at interfaces of hydrophobic and hydrophilic compounds. This is done to minimize the bending energy associated with their spherical curvatures. Deviations from spherical occur when the volume enclosed by the membrane is less than that described by a sphere. For example, the biconcave disc of human erythrocytes deviates from spherical, thus enabling it to bend through capillaries. Helfrich membrane theory, first proposed in 1973, first characterized this bending energy of lipid bilayer membranes as an elastic membrane with three energy components: stretching, tilting, and curving, by deriving quantitative relationships[51]. Through these relationships, he argued that the curvature of a closed vesicle (or cell) is the most important factor to consider for nonspherical vesicle[51,52]:

$$E_{bend} = \oiint_{membrane} \frac{1}{2}\kappa(K - c_O)^2 + \bar{\kappa}K_G \, dA \quad \textbf{(10)}$$

where E_{bend} is the bending energy of the membrane, κ is the bending modulus, K is the mean curvature of the membrane, c_O is the spontaneous curvature of the membrane, $\overline{\kappa}$ is the Gaussian curvature modulus, and K_G is the Gaussian curvature. Helfrich also worked through two theoretical experiments: deformation by magnetic field and by pressure, where the stress due to these deformations can be influenced by the curvature equations[51].

Helfrich membrane theory has proved to be the basis for several other developments about the energetics of lipid bilayer membranes. In his seminal paper, Helfrich noted that a critical assumption, ignoring apparent lipid rafts that cause the membrane to be defined as liquid-crystal rather than simply liquid, simplifies his calculations but may not be accurate[51]. As the name suggests, liquid-crystal states have properties of both liquids and crystalline solids. After Helfrich's original work, it was determined that biological membranes are an example of liquid crystals because the constituent lipid molecules flow easily past one another, but their overall head-tail orientation stays rigid and perpendicular to the membrane plane[53]. Later research showed that shape equations defining both the sphere and the biconcave

disc satisfy the energy equations first put forth by Helfrich, explaining the unique shape of erythrocytes[54]. Importantly, this discovery validates the use of Helfrich membrane theory as a foundation for membrane energy analysis of erythrocytes.

Critically, these discoveries led to a number of assumptions that alter **(10)**. Spontaneous curvature would be nonzero if the membrane has an inherent, spontaneous bend; in biology, this is common as inner and outer leaflets may have different lipid compositions. However, for the planer portions of cell membranes it is often simpler to assume c_O is zero, and this assumption leads to negligible error. Additionally, for a closed surface with no boundary, such as a closed cell membrane, the surface integral of a Gaussian curvature can be written as a topological constant, according to the Gauss-Bonnet theorem[55], which will not affect later physics. Thus, **(10)** can be simplified to:

$$E_{bend} = \oiint_{membrane} \frac{1}{2}\kappa(K)^2 dA \qquad \textbf{(11)}$$

Fluctuations in the membrane, however, transform the smooth membrane surface from two dimensions to three. In order to perform a surface integral, the membrane surface must be parametrized. The Monge parametrization is a straightforward method where the height *h* of a three-dimensional surface relative to a two dimensional reference is given as a function of two coordinates *(x,y)* such that $h = h(x, y)$. Using this method, finite areas are given by:

$$dA = \sqrt{1 + (\nabla h)^2}\,dxdy \approx \left(1 + \frac{1}{2}(\nabla h)^2\right) dxdy \qquad \textbf{(12)}$$

A useful property of the Monge parameterization is for very small gradients, the radical can be approximated as shown. Importantly, cell membranes resist areal increases due to changes in curvature (represented as height in the Monge parametrization) according to a surface tension Σ. This can be understood as a result of the hydrophobic/hydrophilic interactions and steric hindrance discussed previously. Finally, using the Monge parameterization, the mean curvature *K* can be written as the Laplacian of *h*. Accounting for this surface tension, the bending energy of a membrane can finally be written as:

$$E_{bend} = \frac{1}{2}\iint_{membrane} \kappa(\Delta h)^2 + \Sigma(\nabla h)^2 \, dxdy \quad \textbf{(12)}$$

which is a commonly seen form of the Helfrich equation[56].

Chapter 3 – Current Techniques for Measuring Bending Rigidity

Membrane bending rigidity has been a focus of investigation for several decades, with some of the earliest work occurring in the 1970s. With the advent of computer modeling, many of these methods were also validated against theoretical models that could describe the physical phenomena corresponding to the observed mechanical parameters. This section details methods of membrane analysis of synthetic lipid bilayers and cell membranes; methods of analysis are divided into three sections: contact-based methods, non-contact based methods, and simulation/computational methods.

Section 3.1 Contact Based Techniques of Membrane Analysis

Evan Evans pioneered much of the earliest work in determining the mechanical properties of lipid bilayers through micro-mechanical manipulation via a micropipette. Briefly, a glass pipette is heated, stretched, and broken cleanly to generate a smooth, micron-scale diameter orifice; this pipette is then placed against the cell membrane as a suction force is applied. The membrane is drawn into the pipette and the bending modulus is obtained based on the relationship between the aspiration force and displacement [57]. Using this technique, the bending modulus of certain synthetic membranes[58–60] and erythrocyte discocytes[61] can be determined. Advantages of this technique are the ease and low cost, making it widespread even today. Additionally, it serves as the functional basis for micropipettes with nanometer-level diameters on the order of single phospholipid areas; this method is particularly novel for its ability to probe single lipid molecule scale membrane mechanics[35].

Many methods developed more recently take advantage of high energy beams, such as neutron or x-ray, to observe the interactions of lipids in the membrane. While areal analysis does not require contact between methods, as will be discussed later, mechanical analysis often involves stacking membranes in an orientated fashion to observe membrane bilayer interactions with other surfaces. X-ray scattering methods were adapted to determine bending modulus by observing such interactions of lipids[62,63]. Similarly,

neutron beam scattering data was processed uniquely in a neutron spin echo analysis to observe the mechanical properties of stacks of lipid membranes[5].

Erythrocytes are noted to flicker when viewed optically due to the thermal fluctuations of the lipid membrane, and some researchers have devised methods of capturing this flicker data and processing it to obtain mechanical parameters. In one such method, the two-dimensional contour of a flickering giant unilamelar vesicle membrane is captured on camera, cleaned and processed computationally, and analyzed to produce a bending modulus[64]. The use of light optics to determine cell membrane mechanics is still a popular technique. Using a modified differential interference contrast spectroscopy setup, the interference between a reference and object ray reflected from a surface is measured. However, as these rays reflect off a flickering membrane, the interference pattern changes allowing for the measurement of the different wave vectors of membrane flickering[65]. A final optical based technique does not measure the interference of two rays, but rather uses a low-power optical trap and carefully positioned erythrocyte. In this method, the beam of the laser is placed immediately adjacent to the neutral surface of a cell; as flickering occurs, the beam is partially blocked and recorded[8,9]. This optical trap method is reviewed in greater detail later.

Section 3.2 Non-contact Based Techniques of Membrane Analysis

Noncontact methods are a newer area of membrane analysis compared to contact methods, as they frequently require advanced imaging and computational analysis techniques that have only recently become available to membrane researchers.

Similar to the aforementioned optics, diffraction phase microscopy uses principles of interference to measure the thickness of a cell; as the membrane plane fluctuates normal to the light path, interference patterns can be used to construct a dynamic model of cell thickness and membrane height[66]. Critically, however, this technique is performed rapidly enough that free floating cells can be imaged. Additional

phase techniques include phase microscopy based on the Hilbert transform of data, so that phase images can be generated from single signals eliminating the need for a cell to be stuck to a coverslip[67].

In other cases, researchers use high-energy beams to observe the structure of the cell membrane by recording the scattering pattern of beans. In general, these high-energy beams are aimed at a sample of lipids to obtain structure information. In the mid and late 1990s, researchers, led by Nagle, developed methods of using x-ray scattering to observe fully hydrated lipids to determine lipid areas[68] and membrane structure and organization[69–71]. Kučerka *et al*. originally developed a modified small angle neutron scattering technique to observe the bilayer thickness and area of lipid membranes in synthetic vesicles[4,71,72] and have also conducted x-ray scattering investigation[73].

Section 3.3 Computational and Simulation Techniques of Membrane Analysis

Experimental analysis methods provide real data in scenarios that often clearly mirror the real environment of membranes in biology, more so than computational or simulation models. However, computational models have the key advantage of being able to view clear and simple renderings of the true interactions and reactions of molecules. Advancements in physics and chemistry as well as computing power have also helped these models move from theoretical equations to highly accurate simulations and animations.

Early computational models for lipid membranes make many simplifications and assumptions to reduce the necessary computing power without sacrificing significant accuracy of the model. For example, lipids are commonly approximated as hard cylinders or cylindrical springs with varying degrees of complexity. The spring-like definition allows for molecular vibration, stretching, and deformation but the cylindrical shape defines the rough average area that is carved out by lipids in a membrane. Lenz and Schmid have developed a relatively large scale model that uses coarse-grained lipids structured as a spring-like tail and large bead-like head; including some tens of thousands of lipids prevents accurate

single molecule descriptions but accurately describes the general characteristics of a full bilayer[74]. Coarse-grained models are very popular for their low computational demand compared to all-atom models; in an effort to even further reduce computational demand, many researchers are developing models where the solvent surrounding a lipid membrane (almost always water) is implicitly defined in the model, rather than explicitly computed as separate beads or molecules[75]. Despite these simplifications, researchers have developed novel computational approaches to estimate bending modulus and lipid area. Chacón *et al.* have introduced a coupled undulatory mode that removes high wave number modes that do not contribute to lipid area, vastly simplifying the computational demand[76]. While these models are low in computational demand and provide reasonably accurate pictures of membrane dynamics, increasing computational power following Moore's Law has proven capable of allowing for the development of much more sophisticated and accurate simulations.

Other researchers have taken advantage of advancements in computational power to developing fully atomistic molecular simulations. Generally, these methods model lipid molecules down to the atomic level; that is, lipids are modeled down to their covalent bond structure between carbons and hydrogens and other atomic constituents. These highly detailed molecules are then built into lipid bilayer structures and allowed to interact according to known chemical and physical laws, often times foundationally based in Helfrich membrane theory. These molecular dynamics models provide increasingly accurate pictures of membrane structure and mechanical parameters such as bending modulus[77,78].

A hybrid approach, known as single chain mean field theory, uses coarse-grained models of lipid molecules to determine molecular conformations in the most common, mean field force fields observed in membranes. In this way, the most common lipid conformations are determined and mean bilayer conformations are calculated as the weighted average of these individual conformations. Accurate structural information and mechanical parameters have been obtained from single chain mean field theory

using a wide range of grains, from very rapid and coarse three bead per lipid simuluations[79] to more detailed membranes composed of a variety of interacting lipids[80].

Chapter 4 – Methods

Analysis of the physical characteristics of membranes have long been a focus of researchers. Some of the earliest methods by Evans involve micropipette aspiration of the erythrocyte membrane, first hypothesized in the early 1970s[57] and later performed in the early 1980s[61]. Since then, a number of new techniques have been developed that are simpler to perform and impart less stress on the cell membrane. One novel technique is the use of time-correlated single photon counting to observe membrane fluctuations via lifetime fluctuations of embedded fluorophores developed by Butler; validating this technique for cell membranes is a focus of this thesis. Recently, Betz and Sykes have published a method for using a low-power optical trap[8,9]. Given the relative ease of setting up an optical trap, this technique has the potential for widespread use. This chapter will discuss in detail the device setup, cell treatment, and data processing steps for using TCSPC to measure membrane bending modulus. It also provides comprehensive summary for using LPOT as a comparison model.

Section 4.1 Using TCSPC to Characterize Membrane Bending

As discussed above, TCSPC can measure microtimes of excited fluorophores. These fluorophores are highly sensitive to their local environment: different conditions can have significant effects on the nonradiative decay rate and therefore on the observed fluorescent lifetime. The physical environment most likely to change in a bending membrane is the free area per lipid, a measure of average open space surrounding a molecule that increases or decreases as the membrane curves. The following subsections detail the mathematical relationship between lifetime, free area, and mechanical parameters such as bending modulus; the staining protocol for erythrocytes; and the process and assumptions made in

processing raw lifetime data into membrane bending modulus. This method for bending modulus analysis is notable because erythrocytes a free-floating in suspension; therefore, it is a non-contact method membrane analysis. Lifetime of DiI is collected using Becker & Hickl's SPCM software and analyzed via MATLAB.

Section 4.1.1 Derivation of Relationship between Lipid-Free Area, Embedded Fluorophore Lifetime, and Membrane Bending Modulus

The Loufty-Arnold relationship **(13)** describes the changes in nonradiative decay as a function of free volume surrounding a fluorophore and an inherent nonradiative decay reference[81]:

$$K_{nr} = K_{nr}^{o} e^{\frac{-xV_o}{V_f}} \quad \textbf{(13)}$$

where x is a fluorophore-dependent constant, V_O is the hard core volume, and V_f is the free volume. Hard core volume is the volume directly occupied by the lone molecule without any additional environment, for example without water hydrogen bonding around a polar molecule. Using the relationship between radiative decay rate, nonradiative decay rate, and lifetime described in **(6)**, a relationship between free volume and lifetime can be written. Additionally, if lipids are assumed to occupy roughly cylindrical volumes, V can be written as the product of some lipid face area and length. As membranes bend, the free area around a lipid will change; however, there is no analogous "free length" that will change as separation between membrane leaflets is strongly limited by hydrophobic interactions. Combing this, **(13)** can be rewritten as:

$$A_f = \frac{xA_o}{\ln(K_{nr}^{o}) - \ln\left(\frac{1}{\tau} - K_r\right)} \quad \textbf{(14)}$$

where A_f is the free area and A_O is the analogous hard core area. This provides a method for converting lifetime to free area.

An important consideration must be made here. This equation suggests single measurements of lifetime can be converted one-for-one to single measurements of free area. However, a particular microtime in an unstressed environment can still widely vary around the true lifetime; the above discussed method in Section 1.4 for recovering an accurate lifetime requires the averaging of several hundred thousand microtimes. At time scales required for detecting this many photons, the membrane can fluctuate over 9,000 times[82]. As will be shown later, converting free area to bending modulus involves averaging free area fluctuations. Determining individual fluctuations will be impossible if 9,000 fluctuations are averaged down to one value. However, for a sample of several hundred thousand lifetimes, the standard deviation of the lifetime is going to be quite low; most inherent microtime fluctuations are small and very near the true lifetime value. Externally-caused fluctuations, such as those from changes in free area, will have a much greater effect than the majority of these small natural fluctuations and thus the small fluctuations are negligible. Additionally, while very large natural fluctuations are not unheard of, they are much less common in a sample of hundreds of thousands of photons and their effect on the averaging is also negligible. Thus, the vast majority of photon microtimes can be converted to area, one-for-one, with high accuracy.

That being said, several different methods of binning were attempted in order to confirm this hypothesis. Results from binning photons according to both a minimum bin size (in order to achieve a certain accuracy in lifetime) and a maximum bin time length (in order to achieve a certain effective sampling frequency) are presented later. In the case of minimum time length, the macrotimes associated with each photon are summed and checked against an absolutely macrotime maximum in order to ensure each bin represents less than a certain time length.

This represents only the first half of the conversion. Now, free area must be correlated to bending modulus. First, the Helfrich equation **(12)** can be expressed in Fourier space as:

$$E_{bend} = \frac{1}{2}\frac{A^2}{4\pi^2}\iint_{membrane}(\kappa q^4 + \Sigma q^2)h(\boldsymbol{q})h^*(\boldsymbol{q})d\boldsymbol{q} \quad \textbf{(15)}$$

where *A* is the membrane area and $\boldsymbol{q}$ is a two-dimensional Fourier space vector equal to the smallest observable fluctuation, a single molecule, and the largest observable fluctuation, limited by the width of the observation area. Using the equipartition theorem, this can be further modified to:

$$\langle |h(q)|^2 \rangle = \langle h(\mathbf{q}) h^*(\mathbf{q}) \rangle = \frac{k_B T}{A(\kappa q^4 + \Sigma q^2)} \quad \textbf{(16)}$$

Taking the Fourier transform of the Monge representation of membrane height, it is also possible to show:

$$\langle (\nabla^2 h)^2 \rangle = \left(\frac{A}{4\pi^2}\right) \int_{\boldsymbol{\Omega_q}} (\boldsymbol{q}^4) \langle h(\boldsymbol{q}) h^*(\boldsymbol{q}) \rangle d\boldsymbol{q} \quad \textbf{(17)}$$

By solving for area *A* in **(16)** and substituting into **(17)**, the following relationship is found:

$$\langle (\nabla^2 h)^2 \rangle = \left(\frac{1}{4\pi^2}\right) \int_{\boldsymbol{\Omega_q}} \frac{k_b T q^2}{\kappa q^2 + \Sigma} d\boldsymbol{q} \quad \textbf{(18)}$$

The integral of a two dimensional vector $\boldsymbol{q}$ can be simplified to the integral area such that $\int d\boldsymbol{q} = 2\pi \int q dq$ for a circular face. This causes the relationship to simplify to:

$$\langle (\nabla^2 h)^2 \rangle = \left(\frac{k_b T}{2\pi\kappa}\right) \int_{\boldsymbol{2\pi/L}}^{\boldsymbol{2\pi/b}} \frac{q^3}{q^2 + B} d\boldsymbol{q} \quad \textbf{(19)}$$

where *b* is the molecular spacing between lipids, *L* is the membrane length (or maximum observable length), and *B* is the ratio of tension to bending modulus. Integrating gives:

$$\langle (\nabla^2 h)^2 \rangle = \left(\frac{k_b T}{4\pi\kappa}\right) \left[\left(\frac{2\pi}{b}\right)^2 - \left(\frac{2\pi}{L}\right)^2 - B ln \left(\frac{\left(\frac{2\pi}{b}\right)^2 + B}{\left(\frac{2\pi}{L}\right)^2 + B} \right) \right] \quad \textbf{(20)}$$

Seifert has shown that the fluctuations in gradient of height in the Monge parameterization is related to membrane free area fluctuations in[83]:

$$\left\langle \left(\frac{\Delta A_f}{A_f}\right)^2 \right\rangle = \left(\frac{d}{2}\right)^2 \langle (\nabla^2 h)^2 \rangle \quad \textbf{(21)}$$

where *d* is the distance between lipid heads. Combining **(20)** and **(21)** now yields a relationship between free area and bending modulus:

$$\left\langle \left(\frac{\Delta A_f}{A_f}\right)^2 \right\rangle = \left(\frac{d}{2}\right)^2 \left(\frac{k_b T}{4\pi\kappa}\right) \left[\left(\frac{2\pi}{b}\right)^2 - \left(\frac{2\pi}{L}\right)^2 - B ln \left(\frac{\left(\frac{2\pi}{b}\right)^2 + B}{\left(\frac{2\pi}{L}\right)^2 + B} \right) \right] \quad \textbf{(22)}$$

While it is possible to continue manipulation by substituting free area fluctuations for lifetime fluctuations according to **(14)**, this requires the averaging lifetimes. As discussed above, averaging lifetimes causes many fluctuations to be flattened into one measurement and does not provide an accurate measure of bending modulus. Some steps of this derivation are omitted in this section; a full derivation is provided in Appendix A. Based on sample data, there is a clear and sensitive relationship between the bending modulus of cell membranes and free area fluctuations, as seen in figure 4.1.

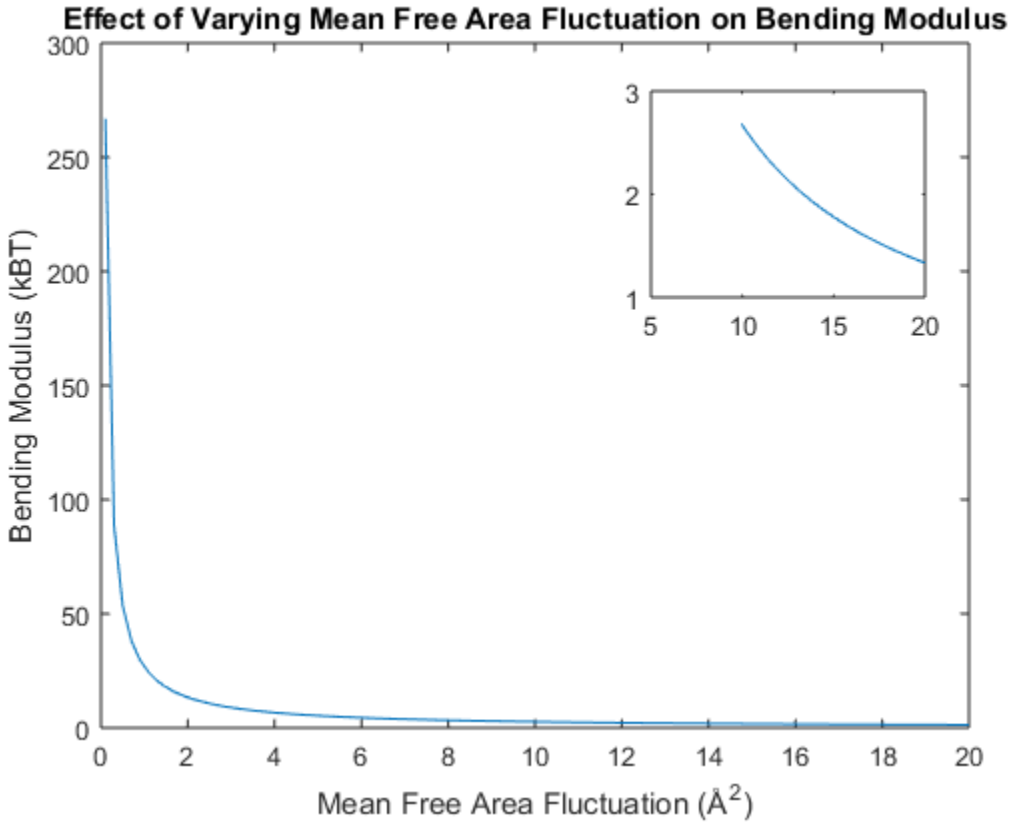

Figure 4.1 Relationshio between Bendning Modulus and Free Area Fluctuations

Section 4.1.2 Staining Erythrocytes with DiI-C_{18}

The above analysis is dependent on a fluorescent sample being embedded in lipid membranes, as biological membranes themselves are not fluorescent. 1'-dioctadecyl-3,3,3'3'-tetramethylindocarbocyanine perchlorate (DiI) and other related compounds are commonly used for membrane staining for a variety of biological applications. The fluorescent DiI head is hydrophilic can be attached to different hydrophobic alkyl chains. Different chain lengths will direct the DiI to different membrane locations according to the lipid raft theory of membrane structure[84]. DiI-C_{18} in solution (ThermoFischer V22855) is used to stain human erythrocytes (hRBC) as it represents a mean chain length that will not be directed exclusively into one lipid raft domain.

Packed hRBCs are diluted to a working concentration of 10,000,000 cells per mL in DulBecco's phosphate buffered saline (Corning 21-030). DiI is added to this solution to obtain a concentration of 1 μM and cells are incubated at 37 °C for 30 minutes. The solution is then centrifuged three times at 3000 rpm for 5 minutes, each time discarding the supernatant and refreshing with new DPBS. The final packed pellet of hRBC are refreshed with a 1% sterile bovine serum albumin (BSA) solution in 1x DBPS. Cells are analyzed within 24 hours of staining and may be lightly vortexed if aggregates appear present. IRF samples are obtained with a 0.2 M solution of Rhodamine B in methanol.

Section 4.1.3 Collecting and Processing Lifetime and Free Area Fluctuation Data

Becker & Hickl's SPCM program is capable of outputting raw microtime values for photons collected in a given file. Typically, photons are collected in batches of approximately 260,000 events. However, these microtimes are still convoluted with the IRF as discussed above. While deconvolution is used for determining the lifetime of a fluorophore based on a large collection of microtimes, previous discussion showed that free area requires a one-for-one conversion of microtimes and therefore another method of removing the IRF is necessary. Alternatively, method of moments is an accurate method of

estimating lifetime from microtime. Photons of both data and IRF arrive according to a Poisson distribution. The first moment of such a distribution is the mean of the data. Subtracting the first moment of the IRF from the first moment of the data file provides an accurate value for lifetime comparable to deconvolution.

In order to calculate bending modulus of a stained hRBC, microtimes in arbitrary units are imported into MATLAB and converted to microtimes in nanoseconds according to a conversion factor provided by SPCM. Each microtime then converted to a free area according to **(14)**. Parameters for DiI are given in the following table.

Table 4.1. Parameters for Converting Lifetime to Free Area

Parameter	Value
Hard core area A_O	42 Å^2
Radiative Decay Rate K_r	0.1590 ns^{-1}
Nonradiative Decay Rate K_{nr}	4.3319 ns^{-1}
Molecular constant x	0.33

After converting lifetimes to an array of free areas, the mean free area is calculated and the mean square fluctuation around that mean is calculated according to **(22)**. This mean fluctuation is then converted to a bending modulus according to a simplified version of **(22)** given below:

$$\left\langle \left(\frac{\Delta A_f}{A_f}\right)^2 \right\rangle = \left(\frac{d}{2}\right)^2 \left(\frac{k_b T}{4\pi\kappa}\right) \left[\left(\frac{2\pi}{b}\right)^2 - \left(\frac{2\pi}{L}\right)^2\right] \quad \textbf{(23)}$$

The value B is omitted because the ratio of tension to bending modulus is much smaller than the other two terms in brackets; B is on the order of 10^{12} while b and L are given in the table 4.2.

The two other terms in the brackets are 6 orders of magnitude larger and thus, the final term can be dropped. While this limits the equation to only solve for bending modulus, it simplifies the equation to one no longer implicit in κ. Moreover, the characteristic length of the largest wave L can be omitted from the equation with little impact, according to figure 4.2. However, L is easy to determine according to the maximum size of the vesicle or confocal laser radius; more appropriately, the lack of sensitivity to L

suggests that fluctuations from all sizes vesicles, from nanoliposomes to large cells, can be fit according to this equation. Experiments are performed at 25 °C.

Table 4.2. Parameters for Converting Free Area to Bending Modulus

Parameter	Value
DiI leaflet spacing *d*	2.74 nm
Molecular spacing *b*	0.47 nm
Characteristic length *L*	1000 nm

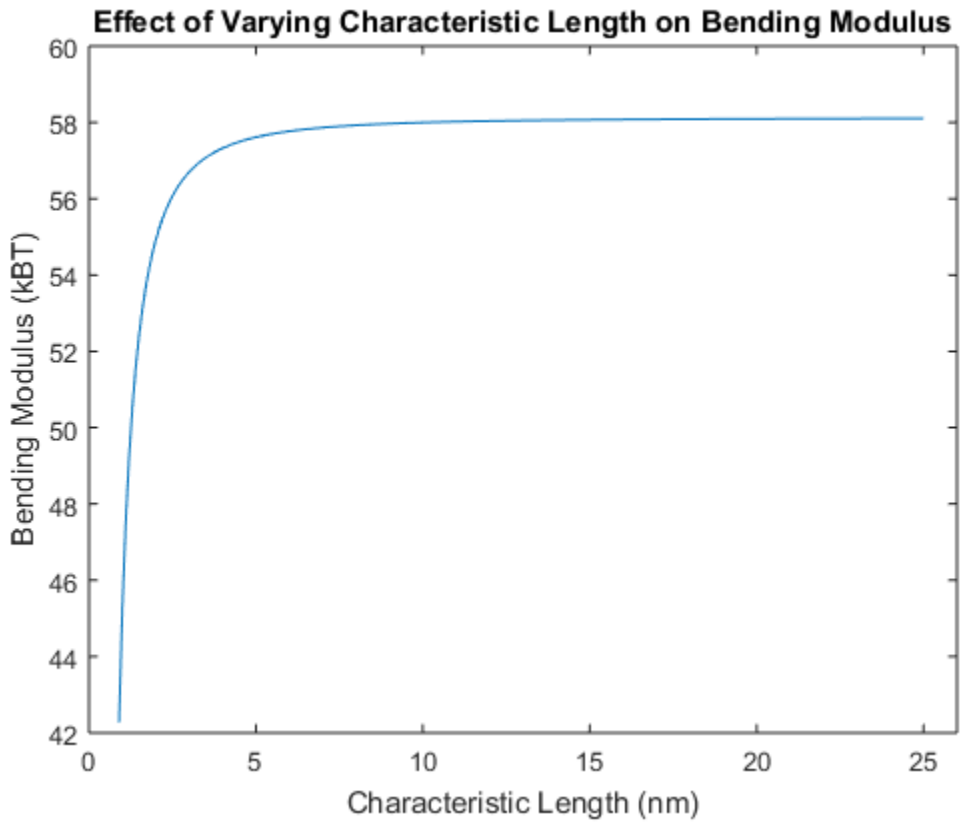

Figure 4.2 Relationship between Bending Modulus and Characteristic Length

Section 4.2 Using LPOT to Characterize Membrane Bending

Section 4.2.1 Preparing Erythrocyte Sample Chamber

A small coverslip is base washed with 0.2 M sodium hydroxide and allowed to dry. They are then coated with a 1% poly-L-lysine solution for 5 minutes before being allowed to dry overnight before attaching cells. A low concentration of poly-L-lysine is used to prevent complete attachment of cells to the glass, which would prevent membrane flickering. Small fluid chambers are prepared by attaching the poly-L-lysine coverslips to a glass microscope slide via double-sided tape; the thickness of the tape ensures an open volume between the two pieces of glass. Solution containing erythrocytes are then loaded into the space and remaining open sides are sealed to prevent any flow of solution or contamination. The chambers are left hanging such that the poly-L-lysine coated coverslip is on the underside of the glass microscope slide, so that cells will be drawn and potentially stick to the surface.

Section 4.2.2 Collecting and Processing Membrane Fluctuation Data

Betz and Sykes have developed a method of using a lower power optical trap to detect membrane fluctuations and correlate those fluctuations to mechanical properties, including membrane bending modulus[8,9]. In their setup, an optical trap is operated at powers that are several orders of magnitude lower than powers required for a trapping effect so that no force is generated by the laser. The laser light is collected by a quadrant photodiode (QPD) that detect fluctuations in the laser on the xy-plane. Such fluctuations may be the result of a lipid membrane fluctuating into and out of the laser path, thus interfering with the photon path. By carefully measuring stepwise changes in QPD voltage signal relative to a controlled distance step from solution across the membrane into the intracellular (or intravesicular) space, a conversion factor between QPD voltage fluctuations and membrane distance fluctuations is obtained. Betz and Sykes have reported a method of collecting time samples of these membrane

fluctuations, calculating a power spectral density (PSD), and fitting the PSD to a theoretical equation based on Helfrich membrane theory:

$$PSD = \sum_{l=2}^{l_{max}} \langle |u_{lm}|^2 \rangle \frac{\omega_l}{\omega_l^2 + \omega^2} \frac{2l+1}{2\pi} \quad \textbf{(24)}$$

where u_{lm} is the fluctuation amplitude of each mode l, given by:

$$\langle |u_{lm}|^2 \rangle = \frac{k_B T}{\kappa(l+2)(l-1)l(l+1) + \Sigma R^2 (l+2)(l-1)} \quad \textbf{(25)}$$

ω_l is the decay frequency of each mode l, given by:

$$\omega_l = \frac{\kappa(l+2)(l-1)l(l+1) + \Sigma R^2 (l+2)(l-1)}{\eta R^3 \frac{(2l+1)(2l^2+2l-1)}{l(l+1)}} \quad \textbf{(26)}$$

and k_B is the Boltzmann constant, T is temperature, κ is the membrane bending modulus, Σ is the membrane surface tension, R is the cell radius, and η is the mean viscosity of the internal and external fluids of the cell[8]. The theory assumes membranes fluctuate in summation of modes, or fluctuation wavelengths. A mode l of one represents the movement of the entire cell and thus the summation begins at the second most. The maximum mode is limited by the resolving power of the microscope setup and is given by:

$$l_{max} \approx \frac{2\pi NR}{0.61\lambda} \quad \textbf{(27)}$$

where N is the numerical aperture of the objective and λ is the wavelength of light[8]. Critically, when conducting data collection, the cell must be stuck to a coverslip and be immobile so that the laser path can sit precisely on the edge of the membrane; this method cannot be used for free-floating cells. A diagram of this setup is shown in figure 4.3.

This experimented was replicated to provide a comparison for data collected via TCSPC. The laser was operated at 98.8 μW, chosen because it gave the most stable zero reading for QPD signal. Previously reported work showed that no influence on mechanical parameters was observed up to 1 mW;

in the setup used for this thesis, no trapping power was observed under 300 μW. Table 4.3 gives the values commonly used for this thesis.

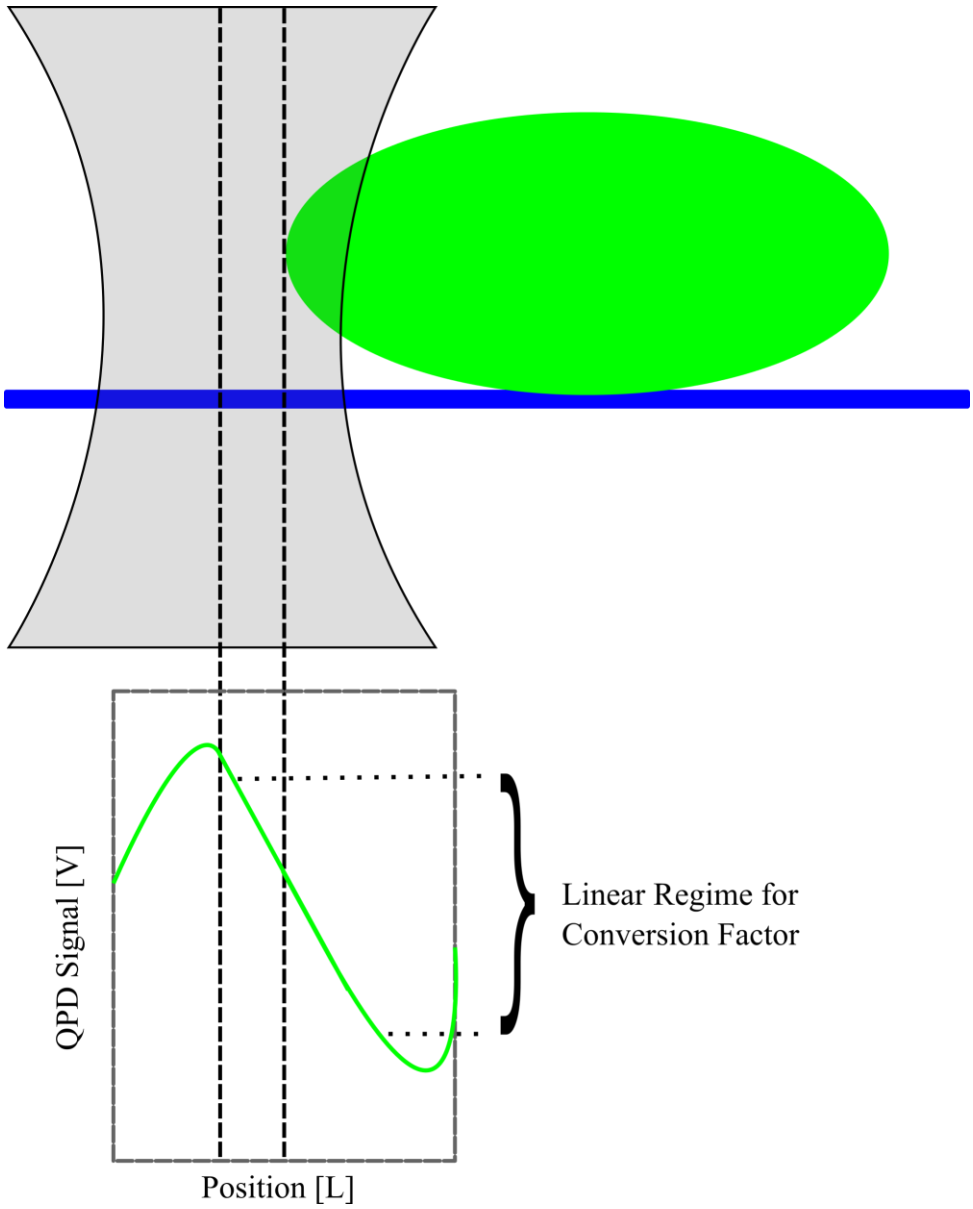

Figure 4.3 Low Power Optical Trap Setup with Calibration Curve

Table 4.3. Setup Parameters for LPOT

Parameter	Value
Temperature *T*	300 K
Cell radius *R*	4 μm
Numerical Aperture *N*	1.2
Wavelength *λ*	1024 nm

Lightly stuck cells were found by observing small areas of contact between the cell and edge of the coverslip while adjusting the z-axis focus. A custom LabView script was used to control the optical trap and obtain a QPD to length conversion factor of 0.524 μm/V; a similar script collected membrane flickering data at a rate of 10,000 Hz for 100,000 QPD signal samples per measurement. One hundred and eight measurements were collected, but only one hundred (n=100) were fitted for bending modulus as the cell showed signs of becoming overly stuck in the last few measurements. A MATLAB program is used to import the raw flickering data, process it into meaningful membrane fluctuation data, filter in via log binning, average all samples collected, and fit the average fluctuation data and frequency data to **(24)**; this program is provided in Appendix C. Data was filtered into thirty-five logarithmically spaced bins. Some components of the program were provided by Timo Betz and modified for use in this thesis.

Chapter 5 – Results

Section 5.1 Bending Modulus Obtained from TCSPC

Two samples of human-derived erythrocytes were stained with DiI according to the aforementioned protocol; one sample was not stabilized with BSA in the final solution. A testing sample of 50 μL was withdrawn from the well-mixed stocks and analyzed via TCSPC. The file size was limited to 1MB in order to collect data over a timespan of 1-2 minutes; this caused each file to contain roughly 260,000 photon samples. Thirteen files were collected without BSA and ten files with BSA. Based on the analysis by the MATLAB programs in Appendix B, the following values were obtained for lifetime (τ), area-per-lipid (APL), and bending modulus (κ) (κ_{FA} is the bending modulus calculated as discussed above and κ_{LT} is the bending modulus calculated if the final substitution of lifetime fluctuations (**14**) is made in **(22)** (mean ± standard deviation):

Table 5.1 Summary of Results for TCSPC Method of Determining Bending Modulus

Parameter	hRBC without 1% BSA (n=13)	hRBC with 1% BSA (n=10)
τ	0.68±0.21 ns	1.40±0.12 ns
APL	43.02±0.94 $Å^2$	44.22±0.45 $Å^2$
κ_{APL}	37.70±4.52 kT	55.60±2.71 kT
κ_{LT}	10.24±7.38 kT	34.78±6.24 kT

For erythrocytes with BSA, values for lifetime are in good agreement with previously reported data[85]. Area-per-lipid of erythrocytes has not been reported in literature, making these data a novel pronouncement. However, a theoretical calculation based on the proportion of phospholipids and cholesterols gives an estimated area of 35.5 $Å^2$ per lipid and 58.5 $Å^2$ for 1:1 combinations of phospholipid and cholesterol[86]. Values for bending modulus are also in good agreement with literature, depending on the model and interpretation. Critically, many sources report a value for bending modulus of ~5 kT for the "bare membrane" or lipid bilayer without spectrin or protein interference, either due to detached spectrin or small area of inspection[35,65,87,88]. However, DiI staining covers the entire membrane of the cell, as seen in figure 5.1, and so values ought to be compared to full cell methods of analysis, which report values

ranging from 30-80 k_BT[9,34,61,67]. It appears that the conversion from lifetime fluctuations to area fluctuations changes the calculated bending modulus, though not out of range of reported values.

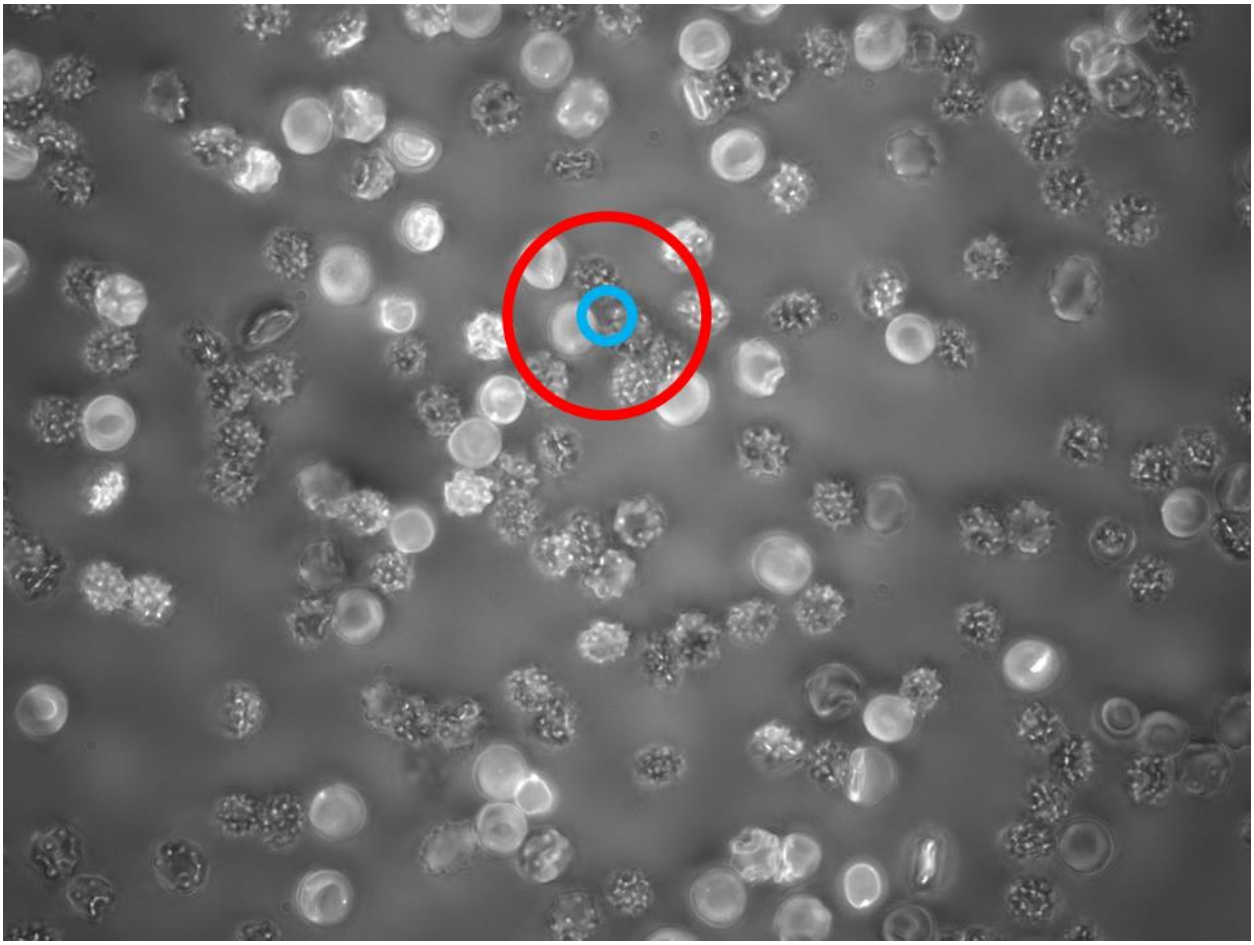

Figure 5.1 Laser focus location on DiI stained erythrocytes

The lack of BSA does lead to a notable number of echinocytes and drastically changes reported parameters compared to healthy discocytes. For data collected, the location of the TCSPC laser focus was noted as exciting both discocytes and echinocytes, as shown in figure 5.1. BSA has known stabilizing effects on membranes, suggesting the mechanical and areal properties have changed. Additionally, the value for lifetime of DiI is highly irregular, likely due averaging signals from discocytes and echinocytes, which have different mechanical properties[65]. Inspecting the cells optically shows that BSA prevents staining as high a proportion of cell membranes, with large clumps of fluorophore forming separate aggregates. This is likely due to the ability of BSA to remove and bind lipids (or lipid analogs such as

DiI) from the membrane[89,90]. However, in the sample with BSA, all fluorescent cells are healthy discocytes and fluorescenct aggregates of BSA and DiI are nonmobile, simplifying the task of inspecting only erythrocytes. BSA is known to modulate area per lipid[91], and this is confirmed in the data presented. This suggests that BSA should be used cautiously in stabilizing DiI stained membranes where measurement of lipid area is critical. These observations are summarized in figures 5.2 and 5.3.

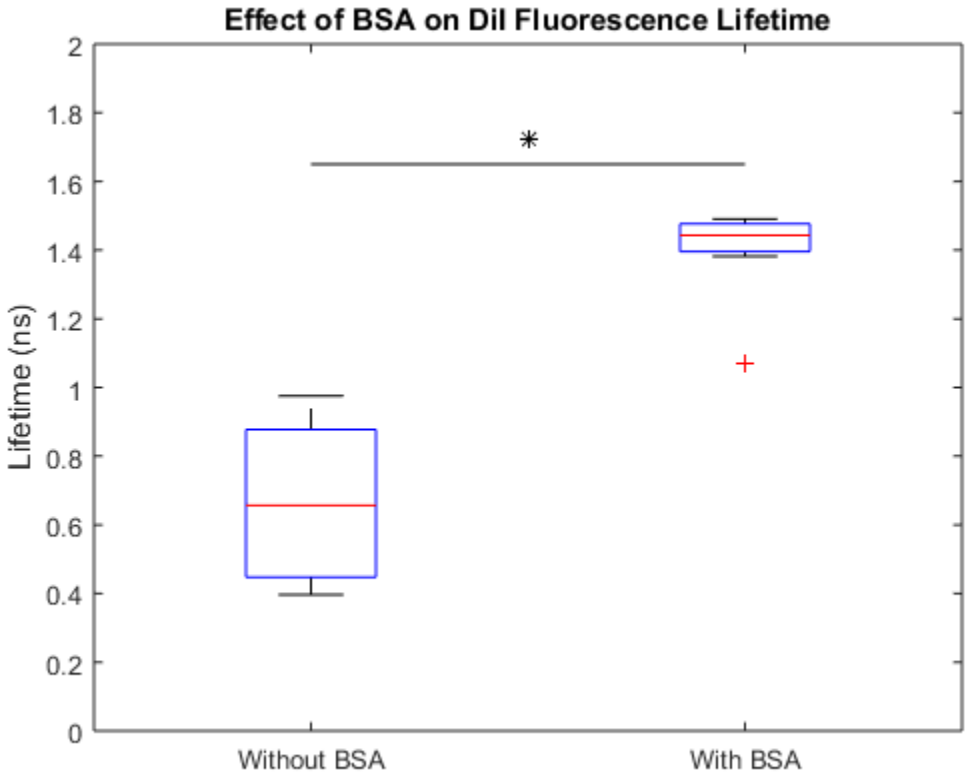

Figure 5.2 Effect of BSA on Lifetime

Additionally, the effect of binning and average photons was investigated. As discussed above, microtimes themselves are not exact representations of lifetime. Lifetime is actually the assigned time constant to the fluorescence decay of a sample. As such, typically a large number of microtimes must be averaged to obtain the true lifetime. Small bins of photons can provide reasonably accurate values of fluorescence lifetime. However, averaging more and more photons leads to a dampening of the

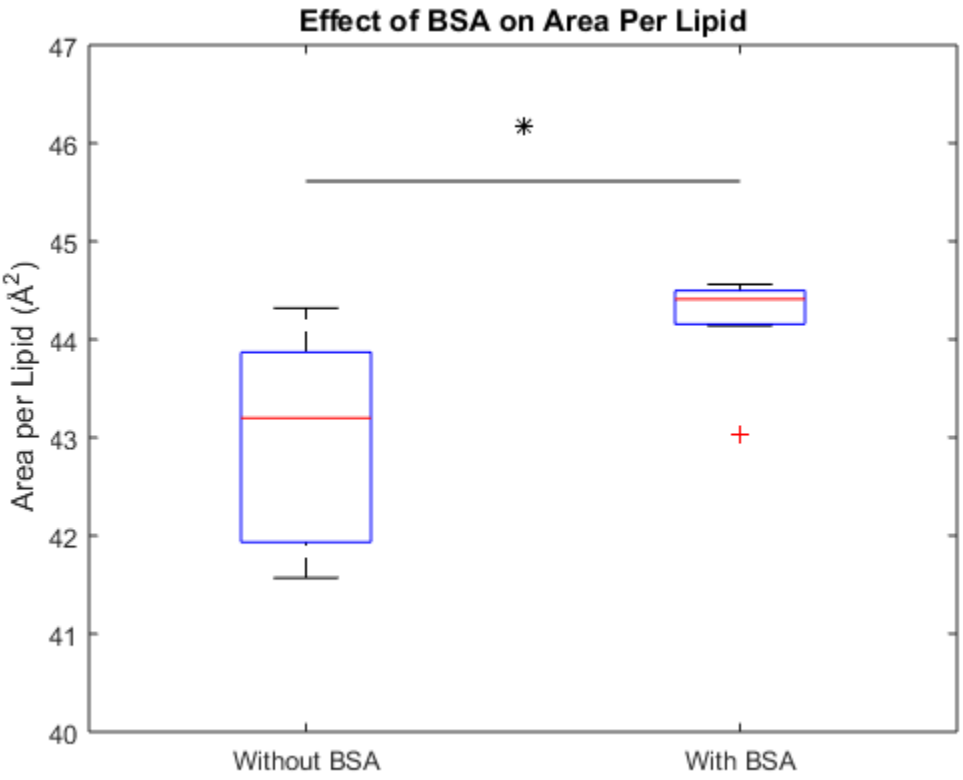

Figure 5.3 Effect of BSA on Area Per Lipid

fluctuations of each photon bin. This in turn causes a smaller and smaller value for mean lifetime fluctuation, which causes the value for bending modulus to rise to infinity, as shown in figure 5.4.

This effect is akin to taking a longer and longer exposure of an image of an erythrocyte. As the time window increases, the position of the membrane trends closer and closer to the average position. Several of these pictures would then show little, if any, fluctuation of membrane position from the mean and would lead to an apparently infinitely stiff bending modulus. While treating microtimes individually as lifetimes is not accurate, for the majority of photons in a large enough sample size of several hundred thousand, the standard deviation of the lifetime is quite low meaning that most of the microtimes are close to the lifetime. Therefore, it is not unreasonable to treat microtimes as lifetimes as it introduces minimal error.

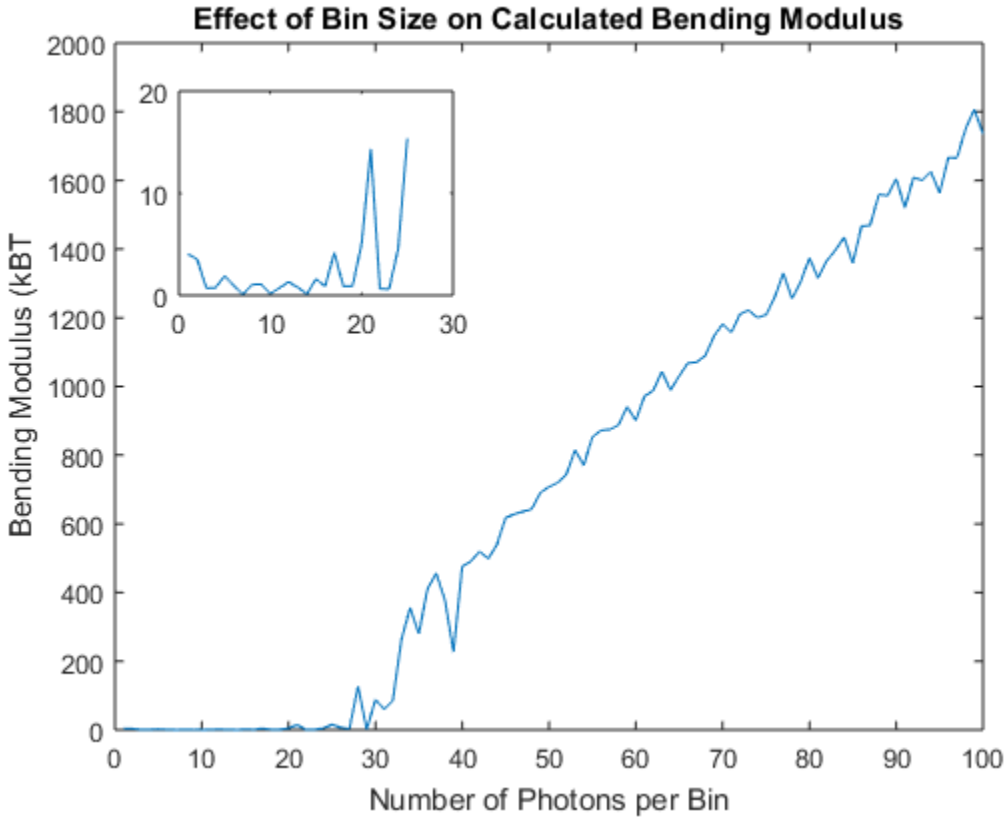

Figure 5.4 Effect of Binning on apparent Bending Modulus

Section 5.2 Bending Modulus Obtained from LPOT

A sample of human-derived erythrocytes were stained with DiI according to the aforementioned protocol and loaded into a coverslip chamber. A sample of 100 measurements, each measurement containing 100,000 QPD signal readings, was collected for analysis. Based on the analysis described in section 4.1.3, the following values were obtained for the bending modulus (κ), membrane tension (σ), and relative viscosity (η) (mean ± standard error):

Table 5.2 Summary of Results for LPOT Method of Determining Bending Modulus

Parameter	Experimental (n=100)	Literature[9] (n=210)
κ	2.87±0.29 $\times 10^{-19}$ J *(69.29 kT)*	2.8±0.2 $\times 10^{-19}$ J *(67.63 kT)*
σ	4.82±0.48 $\times 10^{-7}$ N/m	6.5±2.1 $\times 10^{-7}$ N/m
η	2.55±0.26 $\times 10^{-2}$ Pa·s	8.1±0.4 $\times 10^{-2}$ Pa·s

The calculated bending modulus and surface tension are in excellent agreement with data provided in literature for techniques measuring large membrane area[9,34,61,67], suggesting that the inclusion of DiI in the membrane does not significantly alter the mechanical properties of human erythrocytes. The discrepancy between relative viscosity is noted; however, later discussion will show that the error is due to experimental setup and does not affect the fit accuracy for the other two parameters. Controlling for viscosity at 1.5 cP, the relative value between cellular cytoplasm and water[92,93], recovers similar values for the other mechanical parameters. A plot of the data and fitted power spectrum density is shown in figure 5.5.

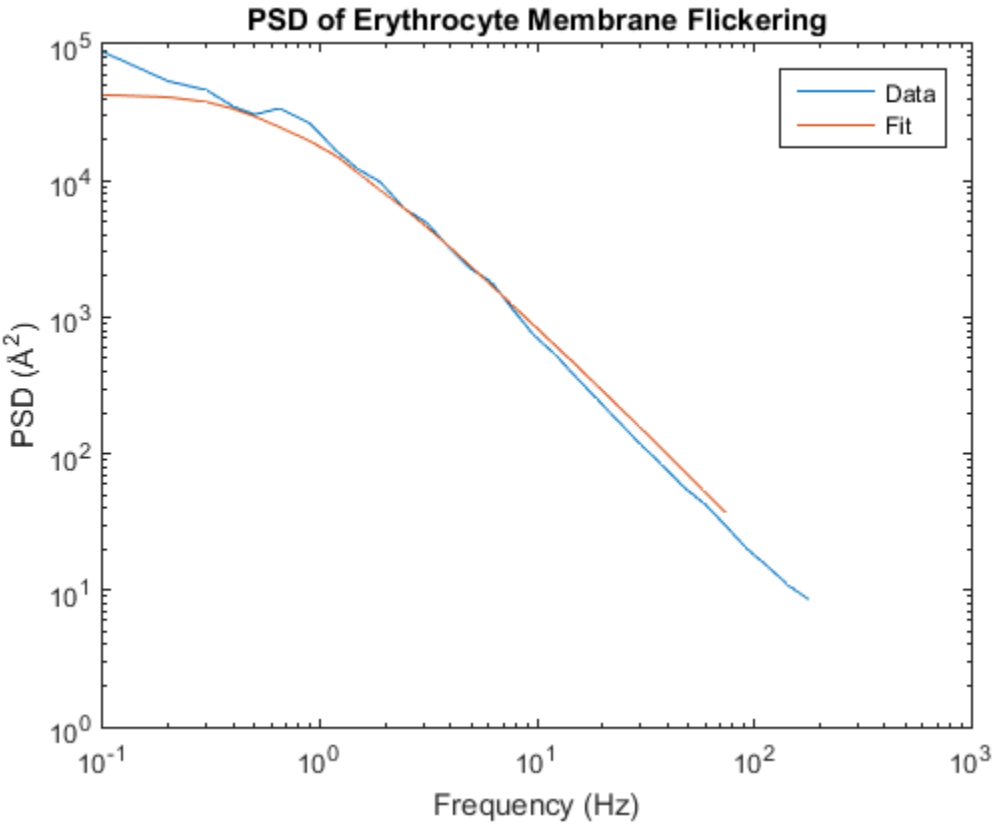

Figure 5.5 PSD Data and Fit

Chapter 6 – Conclusions and Future Work

Erythrocyte mechanics are a highly researched field due to their high flexibility when compared to other eukaryotic, mammalian cells. Due to their importance, significant efforts have gone into characterizing their membrane mechanics. This work demonstrates novel and quick methods for characterizing both small mode and large mode fluctuation of the erythrocyte cell membrane. Compared to other methods reviewed, the use of TCSPC to observe fluorescence lifetime offers several advantages. First, it is able to determine the mean area per lipid of a membrane of unknown composition, which until this point has been only theoretically described for erythrocytes. Additionally, after a simple and common staining procedure, viable cells can be imaged rapidly and accurately. Next, the method does not impact any contact or force on the cells being observed. Finally, and perhaps most importantly, it allows for the inspection of small mode fluctuations uniquely. This final advantage is critical for understanding the effects of membrane mechanics on mechanotransduction, as small membrane fluctuations are more likely to influence lipid-protein and protein-protein behavior.

The DiI staining also shows no significant impact on the mechanics of the cell membrane, as stained cells have similar mechanical parameters to unstained cells reported in literature for both TCSPC and LPOT, for small and large mode fluctuations. This fact, combined with the simplicity of DiI staining, makes the use of TCSPC and fluorescence lifetime an attractive technique for studying the membrane mechanics of many different types of cells in many different environments. TCSPC is conducted on aqueous samples, but otherwise the nature of the sample is not critical. Therefore, experiments at different temperatures, osmolarities, and other factors can be conducted. Additionally, though cells in suspension are ideal for healthy erythrocytes, cells can be stuck to a coverslip surface to model, for example, erythrocyte behavior in blood clotting or to model any number of other cell types in aqueous environments. The relative ease of the technique and lack of assumptions on the nature of the cells being inspect make fluorescence lifetime imaging of the bending modulus attract for further studies.

Communication with Timo Betz has provided insight to the poor fitting ability of the LPOT method for relative viscosity of the internal and external fluids of an erythrocyte. The viscosity is tenfold higher than would be expected for aqueous solutions; however, because the stuck erythrocytes are in such close proximity to the glass coverslip, the external "fluid" viscosity is a combination of a large, low viscosity component (i.e. aqueous solution) and a smaller, infinitely high viscosity component (i.e. glass). Timo Betz has confirmed that for erythrocytes trapped without sticking, much more appropriate values for viscosity are obtained. In both cases, the fitted bending modulus and surface tension are unchanged (*data unpublished*).

Immediate future work may consist of measuring erythrocyte mechanics in different states, such as ATP depletion, or environments, such as non-homeostatic osmolarity. Additionally, adjustment of the MATLAB coding to select certain bins of photons, or effectively changing the sampling frequency, can potentially isolate different modes of membrane fluctuation and reveal subset mechanical parameters that influence the entire behavior. Additionally, different fitting protocols may be able to account for the surface tension, which currently does not have a detectable influence based on the current methods of calculation. Finally, these techniques are easily translatable to measuring the mechanics of endothelial cells in the blood vessel walls to learn about the mechanical parameters and sensitivities to the constant shearing nature of blood flow, among many other mechanically sensitive cells and tissues. Additionally, while not discussed as a result of work in this thesis, other methods of membrane mechanics characterization are possible; for example, this TCSPC technique could be combined with FCS to observe the diffusion of membrane proteins or other membrane-bound entities through mechanically different lipid bilayers or regions.

Chapter 7 – Appendices

Appendix A

Full Derivation of Equation Relating Membrane Bending Modulus to Lifetime Fluctuations

This section provides step-by-step analysis for the derivations referenced in Section 2.1.1. Notes on the right side of the page discuss what action was taken to obtain the mathematical expression on that line. A table of terms and parameters with their definitions is provides at the start.

Table 7.1 List of terms in order of appearance in the derivation

Term	Definition
K_{nr}	non-radiative decay rate
K_{nr}^{o}	torsional non-radiative decay rate in low viscosity environments
x	molecule-dependent constant
V_o	hard-core volume
V_f	free volume
K_r	radiative decay rate
φ	fluorescence quantum yield
τ	fluorescence lifetime
L	characteristic membrane length
A_o	hard-cord area
A_f	free area
h	membrane fluctuation height
Ω	two-dimensional domain of integration
q	wavelength vector in Fourier space equal to $(\frac{2\pi}{b}.\frac{2\pi}{L})$
x	area vector
E_{bend}	membrane bending energy
κ	membrane bending or elastic modulus
Σ	membrane surface tension
k_b	Boltzmann's constant
T	temperature
d	distance between fluorophore dyes
b	molecular spacing distance

(1) $$K_{nr} = K_{nr}^{o} e^{\frac{-xV_o}{V_f}}$$ *Loufty-Arnold relationship for torsional relaxation rate of a fluorophore*

(2) $$K_r = \frac{\varphi}{\tau}$$ *Definition of radiative decay rate*

(3) $$K_{nr} = \frac{1 - \varphi}{\tau}$$ *Definition of non-radiative decay rate*

(4) $$\varphi = K_r \tau$$ *Rearrange (2) to isolate quantum yield*

(5) $$K_{nr} = \frac{1 - K_r \tau}{\tau} = \frac{1}{\tau} - K_r$$ *Use (4) as an identity in (3)*

(6) $$\frac{1}{\tau} - K_r = K_{nr}^{o} e^{\frac{-xV_o}{V_f}}$$ *Use (5) as an identity in (1)*

(7) $$\frac{\frac{1}{\tau} - K_r}{K_{nr}^{o}} = e^{\frac{-xV_o}{V_f}}$$ *Rearrange (division)*

(8) $$ln\left(\frac{\frac{1}{\tau} - K_r}{K_{nr}^{o}}\right) = \frac{-xV_o}{V_f}$$ *Take the logarithm (Exponent identity: $e^{\ln(A)} = A$)*

(9) $$\ln\left(\frac{1}{\tau} - K_r\right) - \ln(K_{nr}^{o}) = \frac{-xV_o}{V_f}$$ *Logarithm identity:* $\ln\left(\frac{A}{B}\right) = \ln(A) - \ln(B)$

(10) $$V_f = \frac{-xV_o}{\ln\left(\frac{1}{\tau} - K_r\right) - \ln(K_{nr}^{o})}$$ *Rearrange to isolate free volume (division)*

(11) $$A_f = \frac{xA_o}{\ln(K_{nr}^o) - \ln\left(\frac{1}{\tau} - K_r\right)}$$

Let some characteristic lipid height $\boldsymbol{H}$ *be* $\boldsymbol{V = AH}$*; Relationship between free area per lipid and lifetime*

(12) $$\frac{dA_f}{d\tau} = \frac{-xA_o}{\left(\frac{1}{\tau} - K_r\right)(\tau^2)\left(\ln(K_{nr}^o) - \ln\left(\frac{1}{\tau} - K_r\right)\right)^2}$$

Differentiate A_f *with respect to* τ

(13) $$\frac{dA_f}{d\tau} = \frac{-A_f}{\tau(1 - \tau K_r)\left(\ln(K_{nr}^o) - \ln\left(\frac{1}{\tau} - K_r\right)\right)}$$

Substitute (11) into (12), distribute τ

(14) $$\frac{dA_f}{A_f} = \frac{-1}{(1 - \tau K_r)\left(\ln(K_{nr}^o) - \ln\left(\frac{1}{\tau} - K_r\right)\right)}\frac{d\tau}{\tau}$$

Split differential (ie implicit)

(15) $$\left(\frac{dA_f}{A_f}\right)^2 = \left(\frac{1}{(1 - \tau K_r)\left(\ln(K_{nr}^o) - \ln\left(\frac{1}{\tau} - K_r\right)\right)}\right)^2\left(\frac{d\tau}{\tau}\right)^2$$

Square all terms

(16) $$\langle\left(\frac{\Delta A_f}{A_{f_o}}\right)^2\rangle = \left(\frac{1}{(1-\tau K_r)\left(\ln(K_{nr}^o) - \ln\left(\frac{1}{\tau} - K_r\right)\right)}\right)^2 \langle\left(\frac{\Delta\tau}{\tau_o}\right)^2\rangle$$

Let fluctuations be large, and average them against the mean values

(17) $$h(x) = \frac{A}{4\pi^2}\int_{\Omega_q} e^{iqx}h(q)dq$$

Fourier transform of Monge representation of membrane height

(18) $$\nabla^2 h(x,t) = \frac{A}{4\pi^2}\int_{\Omega_q}(-q^2)e^{iqx}h(q,t)dq$$

Take the Laplacian of $h(x)$

(19) $$(\nabla^2 h(x,t))^2 = (\nabla^2 h)^2 = \left(\frac{A}{4\pi^2}\right)^2 \iint_{\Omega_q}(q^2 q'^2)e^{iqx}e^{-iq'x}h(q)h^*(q')dqdq'$$

Square both sides of the equation

(20) $$(\nabla^2 h(x,t))^2 = (\nabla^2 h)^2 = \left(\frac{A}{4\pi^2}\right)^2 \iint_{\Omega_q}(q^2 q'^2)e^{iqx-iq'x}h(q)h^*(q')dqdq'$$

Exponent identity: $e^{A+B} = e^A e^B$

(21) $$\langle(\nabla^2 h)^2\rangle = \left(\frac{A}{4\pi^2}\right)^2 \int A^{-1} dx \iint_{\Omega_q} \left(q^2 q'^2\right) e^{iqx - iq'x} \langle h(q) h^*(q')\rangle dq dq'$$

*Perform a positional average (note: **x** is a two-dimensional area vector)*

(22) $$\int e^{iqx - iq'x} dx = 4\pi^2 \delta(q - q')$$

Identity

(23) $$\langle(\nabla^2 h)^2\rangle = \left(\frac{A}{4\pi^2}\right) \iint_{\Omega_q} \left(q^2 q'^2\right) \delta(q - q') \langle h(q) h^*(q')\rangle dq dq'$$

Substitute (22) into (21)

(24) $$\langle(\nabla^2 h)^2\rangle = \left(\frac{A}{4\pi^2}\right) \int_{\Omega_q} \left(q^4\right) \langle h(q) h^*(q \quad)\rangle dq$$

Use the sifting property of the Dirac function

(25) $$E_{bend} = \frac{1}{2} \int_{\Omega_x} \left[\kappa(\Delta h)^2 + \Sigma(\nabla h)^2\right] dx$$

Bending Energy of the membrane

(26) $$E_{bend} = \frac{1}{2}\frac{A^2}{4\pi^2}\int_{\Omega_p}\left(\kappa q^4\right)h(q)h^*(q)dq$$ *Fourier transform of bending energy*

(27) $$E_{bend} = k_bT = \langle h(q)h^*(q)\rangle A\left(\kappa q^4 + \Sigma q^2\right)$$ *Equipartition theorem of bending energy*

(28) $$\langle(\nabla^2 h)^2\rangle = \left(\frac{1}{4\pi^2}\right)\int_{\Omega_q}\frac{k_bTq^2}{\kappa q^2 + \Sigma}dq$$ *Substitute (27) into (26)*

(29) $$\int dq = 2\pi\int q\,dq$$ *Identity based on area of cylindrical face*

(30) $$\langle(\nabla^2 h)^2\rangle = \left(\frac{k_bT}{2\pi\kappa}\right)\int_{2\pi/L}^{2\pi/b}\frac{q^3}{q^2 + B}dq$$ *Substitute (29) into (28); apply integral bounds and simplify, where* $B = \frac{\Sigma}{\kappa}$

(31)

$$\langle(\nabla^2 h)^2\rangle = \left(\frac{k_b T}{4\pi\kappa}\right)\left[\left(\frac{2\pi}{b}\right)^2 - \left(\frac{2\pi}{L}\right)^2 - B ln\left(\frac{\left(\frac{2\pi}{b}\right)^2 + B}{\left(\frac{2\pi}{L}\right)^2 + B}\right)\right]$$

Integrate

(32)

$$\left\langle\left(\frac{\Delta A_f}{A_o}\right)^2\right\rangle = \left(\frac{d}{2}\right)^2 \langle(\nabla^2 h)^2\rangle$$

Siefert Free area fluctuation

(33)

$$\left\langle\left(\frac{\Delta A_f}{A_o}\right)^2\right\rangle = \left(\frac{d}{2}\right)^2 \left(\frac{k_b T}{4\pi\kappa}\right)\left[\left(\frac{2\pi}{b}\right)^2 - \left(\frac{2\pi}{L}\right)^2 - B ln\left(\frac{\left(\frac{2\pi}{b}\right)^2 + B}{\left(\frac{2\pi}{L}\right)^2 + B}\right)\right]$$

Substitute (31) into (32)

(34)

$$\left\langle\left(\frac{\Delta\tau}{\tau_o}\right)^2\right\rangle = \left((1 - \tau K_r)\left(\ln(K_{nr}^o) - \ln\left(\frac{1}{\tau} - K_r\right)\right)\right)^2 \left(\frac{d}{2}\right)^2 \left(\frac{k_b T}{4\pi\kappa}\right)\left[\left(\frac{2\pi}{b}\right)^2 - \left(\frac{2\pi}{L}\right)^2 - B ln\left(\frac{\left(\frac{2\pi}{b}\right)^2 + B}{\left(\frac{2\pi}{L}\right)^2 + B}\right)\right]$$

Substitute (16) into (33)

Appendix B

MATLAB Code for Fitting TCSPC Data for Recovering Membrane Bending Modulus

N.B: MATLAB default-generated font is maintained. Briefly, `this font` implies commenting, which explains code but does not actually affect the program; `this font` implies simple commands, such as common MATLAB expressions or mathematical expressions; `this font` implies characters,

which is text displayed by MATLAB rather that variables to be manipulated; `this font` implies complex MATLAB functions that involve directing variables through loops or switches.

Function: Standard Deviation of Lifetime

```
% Convert IRF data file microtimes to "lifetime" values in nanosecond units
% and determine a first moment ("mean") and standard deviation of the data
% set.

% Written by Nick Frazzette

clear
clc

%% Query Bin Count from SPCM
bin_count=questdlg({'What was the number of bins used to collect
data?','(Click the button using the mouse)'},...  %Query the bin count
                   'Histogram
Binning',...                                      %Title dialog box

'256','4096','4096');                                          %Provide options
    switch
bin_count                                                          %Select
conversion factor based on binning
        case '256'
            conv_fact=0.048857293;
        case '4096'
            conv_fact=0.003053581;
    end

%% Search for IRF ASCII files
filebasename='irf';                           %Label initial letters for base
file
namesearch=strcat(filebasename,'*.asc');      %Search for ASCII files begining
with base name
files=dir(namesearch);                        %Create a directory of files
numfiles=length(files);                       %List number of files being
process

%% Process Microtime Data into Lifetime Bins
name=files(1).name;                                                %Identify
first file to be processed
BMini=load('-ascii', name);                                        %Load all
data (macrotimes, microtimes) from ASCII file
microtimes=BMini(:,2);                                             %Isolate
unprocessed microtimes in arbitrary ps units
clear BMini
lifetime_IRF=(microtimes*conv_fact);

%% Export the standard deviation of the IRF
IRF_mode=mode(lifetime_IRF)
adjusted_IRF=lifetime_IRF-IRF_mode;
```

```
j=1;    %Define an index for the new lifetime array
nv=0;   %Define a counter for the number of values removed
for i=1:length(adjusted_IRF)    %Loop operation for the length of the
lifetime array containing negative values
    if adjusted_IRF(i)<=0       %Direct operation if the current lifetime is
negative or zero
            nv=nv+1;                    %Increase negative values count
        else                            %Direct operation if the current
lifetime is positive
            IRF_array(j)=adjusted_IRF(i); %Insert current lifetime into a new
lifetime array
            j=j+1;                              %Increase new lifetime array
index
        end     %Close if-directory
end         %Close for-loop
sprintf('%d negative values were removed.',nv)  %Export the number of
negative values removed from the lifetime array
clear i j nv    %Clear index and count variables
IRF_m1=mean(IRF_array)
IRF_std=stdev(IRF_array)
```

Function: Bending Modulus Via Free Area

```
%Calculate the bending modulus of a lipid bilayer membrane stained with DiI
%C16 using instantaneous free area per lipid and area fluctuations, based
%on a minimum photon/microtime count necessary to achieve an accurate
%lifetime and accurate instantaneous free area per lipid. See Muddana,
%Huang, et al in Nat Meth B (2015) and Timing Stability of TCSPC
%Experiments from Becker&Hickl.

%Written by Nick Frazzette

clear
clc
tic
%% Query Bin Count from SPCM, First Moment of IRF, and Desired Accuracy
bin_count=questdlg({'What was the number of bins used to collect
data?','(Click the button using the mouse)'},...  %Query the bin count
                    'Histogram
Binning',...                                    %Title dialog box

'256','4096','4096');                                       %Provide options
    switch
bin_count                                                       %Select
conversion factor based on binning
        case '256'
            conv_fact_mic=0.048857293;
        case '4096'
            conv_fact_mic=0.003053581;
    end
off_IRF=input('Enter offset value of IRF in ns.   ');   %Request user input
for the IRF mean
stdev_IRF=input('Enter standard deviation value of IRF in ns.
');    %Request user input for the IRF standard deviation
```

```
temp=input('Enter the measurement temperature in Celsius.    ');

%% Search for Bending Modulus ASCII files
filebasename='';                              %Label initial letters for base
file
namesearch=strcat(filebasename,'*.asc');      %Search for ASCII files begining
with base name
files=dir(namesearch);                        %Create a directory of files
numfiles=length(files);                       %List number of files being
process

for i=1:numfiles %Use for-loop to calculate the mechanical parameters for
each file collected
    %% Process Microtime Data into Lifetime Data
    name=files(i).name;                   %Identify first file to be processed
    BMini=load('-ascii', name);           %Load all data (macrotimes,
microtimes) from ASCII file
    microtimes_au=BMini(:,2);                %Isolate unprocessed microtimes
in arbitrary ps units
    clear BMini                           %Clear large variable to free
program memory
    microtime_with_IRF=(microtimes_au*conv_fact_mic); %Convert microtimes in
AU to microtimes in ns (for 256-bin, factor is 0.048857293 ns/ps; for 4096-
bin, factor is 0.003053581 ns/ps)
    tau=microtime_with_IRF-off_IRF;
    mean_tau(i)=mean(tau)
    stdev_lifetime(i)=stdev_IRF.*sqrt(2/length(tau))          %Export a value
for lifetime standard deviation based on B&H
    %% Convert each Lifetime measurement into an instantaneous Free Area
    Ao=0.42e-18;    %Hardcore lipid area in m^2
    Kr=0.1590;      %Radiative decay rate (1/ns)
    lnKnr0=1.466;   %Natural log of non-radiative decay rate at low viscosity
    x=0.33;         %Molecular constant
    free_area=(x.*Ao)./(lnKnr0-log(1./tau-Kr));           %Calculate the free
area per lipid for each photon bin

    %% Calculate Bending Modulus from Free Area Fluctuations
    d=2.74e-9;      %distance between dye heads in inner and outer membrane
leaflets in m
    b=0.47e-9;      %molecular spacing
    T=temp+273.15;  %temperature in Kelvin
    kB=1.381E-23;   %Boltzmans constant
    L=1000e-9;      %Characteristic length of largest wave
    APL=Ao+free_area;       %Calculate the area per lipid array from free
area array
    APL_m2=abs(mean(APL));  %Calculate the mean area per lipid
    APL_A2(i)=APL_m2*10^20  %Export area per lipid in square angstroms
    FAfluc=mean(((APL_m2-APL)/APL_m2).*conj(((APL_m2-
APL)/APL_m2)));                               %Calculate the mean free area
fluctuations

    %Assumptions are made with the following equation, namely that b^-2 and
L^-2 are sufficiently large to dwarf any additional terms in the parens,
    %and therefore, additional terms are left out from this approximation
```

```
    kappa_J_FA(i)=((d/2)^2)*((kB*T)/(4*pi))*(((2*pi)/b)^2-
(2*pi/L).^2)/(FAfluc)    %Export the bending modulus in joules and KT
    kappa_KT_FA(i)=((d/2)^2)*((1)/(4*pi))*(((2*pi)/b)^2-(2*pi/L).^2)/(FAfluc)

    %% Calculate Bending Modulus from Fluorescence Lifetime
    LTfluc=mean(((mean_tau(i)-
tau)/mean_tau(i)).^2);                      %Calculate the mean lifetime
fluctuation

    F_tau=((1-mean_tau(i)*Kr).*(lnKnr0-log((1/mean_tau(i))-
Kr))).^2;      %Calculate the f(tau) term to simplify later equations

    kappa_J_LT(i)=(F_tau).*((d/2).^2).*(kB*T/4/pi).*((2*pi/b).^2-
(2*pi/L).^2)./(LTfluc)    %Export the bending modulus in joules and KT
    kappa_KT_LT(i)=(F_tau).*((d/2).^2).*(1/4/pi).*((2*pi/b).^2-
(2*pi/L).^2)./(LTfluc)
    clear APL free_area microtime_with_IRF microtime_au tau     %clear large
variables between iterations
end     %close for-loop
toc
```

Appendix C

MATLAB Code for Fitting LPOT Data for Recovering Membrane Bending Modulus

N.B: MATLAB default-generated font is maintained. Briefly, `this font` implies commenting, which explains code but does not actually affect the program; `this font` implies simple commands, such as common MATLAB expressions or mathematical expressions; `this font` implies character strings, which is text displayed by MATLAB rather that variables to be manipulated; `this font` implies complex MATLAB functions that involve directing variables through loops or switches.

Function: PSD Fitter

```
function [] = PSDFitter()
%PSDFitter accepts any number of cell membrane flickering data from the
%optical trap and determines the bending modulus, surface tension, mean
%viscosity, and elastic coupling to spectrin
%   PSDFitter converts raw membrane flickering data from a QPD optical trap
%   set up into a power spectral density function using a Fourier
%   transform. Then, it fits that power spectral density function against a
%   known function derived from Betz and Sykes (2012) by adjusting four
%   constants iteratively. Those four constants have the physical meaning
%   of the membrane bending modulus, surface tension, mean viscosity of
%   cytosol and extracellular fluid, and elastic coupling between the
%   membrane and spectrin network. Fitting is accomplished via a Nelder
%   Mead simplex algorithm to minimize a difference of squares between data
```

```
%   and a theoretical function.

tic
%% Data Processing and Function Development
kB=1.3806488e-23;   %Boltzmann constant [J/K]

disp('All values must be reported in base SI units. Enter only the numerical
value.');
r=4e-6;     %input('Input the cell radius\n');           %for most RBCs 4e-6
m
tem=300;    %input('Input the ambient temperature\n');   %estimated 295.15 K
(i.e. room temperature)
Fs=10000;   %input('Input the sampling frequency\n');     %usually set to
10000 Hz
ConvFactor=input('Input the length to QPD units conversion factor (i.e.
[L]/[QPD])\n'); %taken from calibration curve
k=input('Input the number of samples\n');
BN=input('Input a bin
number\n');                                                    %enter a
number of bins for filtering the data via log binning
fit_array=input('Input the fit array, in the form [sigma kappa eta] where "1"
fits that variable\n');
%fit_array defines which parameters the program will try to fit; for
%example, [1 1 0] will fit sigma and kappa, but consistently pass the
%initial guess for eta

for i=1:k                           %importing an arbitrary ("k") number of
data files as a matrix of k rows
    filename=sprintf('%d.txt',i);   %note: the files must start with "1",
ascend in order, and be text files
    RF(i,:)=load(filename)';        %RF is raw membrane flickering data (in
QPD units)
end
clear i             %clear loop count
fdl=RF.*ConvFactor; %convert the QPD fluctuations to length fluctuations
where FDL is the flickering data converted to length

freq_nocut=linspace(0,Fs,length(fdl(1,:)));                    %generate a
frequency array corresponding to the flickering data
freq_cut=freq_nocut(1:2000);                                   %cut the
array to avoid outliers and oversampling [Nyquist cut>(find(freq_nocut >
(Fs/2),1,'first')-1)]
spacing=round(logspace(log10(1),log10(length(freq_cut)+1),BN)); %generate an
array of bin edges for log binning
[~,binidx]=histc(1:length(freq_cut),spacing);                  %generate an
array of indices to a certain bin for each frequency point
fbinned=accumarray(binidx.',freq_cut',[],@mean)';              %collect and
average all values of frequency within a bin

for i=1:k           %repeat the following process for each data file
collected

FDL(i,:)=fft(fdl(i,:));                                                %conv
ert FDL to frequency domain using a fast Fourier Transform
```

```
PSD_nocut(i,:)=((FDL(i,:).*conj(FDL(i,:))./(Fs.*length(fdl(i,:))));    %comp
ute the Power Spectrum Density (from Betz and Sykes 2012);

PSD(i,:)=PSD_nocut(i,1:2000);                                          %cut
the PSD to match the frequency array

pbinned(i,:)=accumarray(binidx.',PSD(i,:)',[],@mean);                  %coll
ect and average all values of PSD according to previous log binning
end

xdata=fbinned;  %rename variable for use in provided code
for j=1:BN-1    %average all PSD files into one curve, rename for use in
provided code
    ydata(j)=mean(pbinned(:,j));    %calculate the mean of each PSD point
    ydstd(j)=std(pbinned(:,j));     %calculate the standard deviation of each
PSD point
end

lambda=1024e-9;         %laser wavelength in nanometers
NA=1.45;                %numerical aperature of objective
delX=(0.61*lambda)/NA;  %compute the spatial resolution delX of the laser
(i.e. how fine a distance the laser can resolve)

lmin=2;                   %define the lower summation limit (from Betz and
Sykes 2012);
lmax=ceil(2*pi*r/delX);   %compute the upper summation limit

%estimated guesses for kappa, sigma, eta, and gamma (taken from Betz and
Sykes 2012)
kappa=2.8e-19;             % J
s=6.5e-7;                  % N/m
eta=1.7e-3;                % Pa*s
nu=0.06e-8;                % J/m^4

%% Fit Theoretical Curve to Collected Data
start_point = [1e-8 1e-19 1e-2 lmax];   %define an initial guess
model = @modelfun;                      %define a simple function handle for
use in Nelder-Mead function
optnew=optimset('fminsearch');          %define Nelder-Mead fitting
parameters
optnew.TolX=1e-300;                     %maximum difference between data and
fit
optnew.MaxFunEvals=2e9;                 %maximum number of fitting iterations
[estimates,~,flag] = fminsearch(model,
start_point,optnew);              %perform fit

if fit_array(1)==1          %change variables according to fit array (see
above)
    sigma = estimates(1);
else
    sigma=s;
end
```

```
if fit_array(2)==1
    kappa = estimates(2);
else
    kappa=kappa;
end

if fit_array(3)==1
    eta = estimates(3);
else
    eta=eta;
end

estimates   %export the post-fit values
flag        %export the condition for closing the fitting routine

[~,FittedCurve] = modelfun(estimates);  %generate a theoretical PSD graph
based on the post-fit values
        xd=xdata(1:length(FittedCurve));%cut the frequency array to match the
PSD array
        xd(find(FittedCurve==0))=[];    %remove all zero values
        FittedCurve(find(FittedCurve==0))=[];   %remove all zero values
loglog(xdata,ydata,xd,FittedCurve)      %plot the data and theoretical curve

%% Define the Fitting Function
function [sse, FittedCurve] = modelfun(params)
    if fit_array(1)==1  %change variables according to fit array (see above)
        s = params(1)
    else
        s=s;
    end

    if fit_array(2)==1
        k = params(2)
    else
        k=kappa;
    end

    if fit_array(3)==1
        eta = params(3)
    else
        eta=eta;
    end


[f,FittedCurve]=generate_powerspectrum_spherical_harmonics_safran(r,xdata,k,s
,eta,lmax);

    FittedCurve(find(f==0))=[]; %remove zeros from fit array
    yd=ydata(1:length(f));      %cut data array to match length of fit array
    yd(find(f==0))=[];  %remove zeros
    f(find(f==0))=[];   %remove zeros

    ErrorVector = (FittedCurve - yd)./FittedCurve;   %generate an error
vector to minimize
```

```
    ErrorVector(isnan(ErrorVector))=[];              %remove non-number
elements
    sse = 1000000000*abs(sum(abs(ErrorVector) .^ 2));%define residual sum of
squares
end
toc
end
```

Program: PSD Generator

```
    function
[f,S]=generate_powerspectrum_spherical_harmonics_safran(R,f,k,s,eta,l_m)
%This function will generate the expected PSD of the spherical harmonics as
%a function of the radius R, at the frequencies f (1d array), with bending
%modulus k, tension s, viscosity eta, and up to the l_m'th mode.

KT=1.38E-23*300; %adjust temperature as needed

k=abs(k);   %ensure values for bending modulus are positive
s=abs(s);   %ensure values for tension are positive

l=2:round(l_m); %generate array of modes
Z=(2*l+1).*(2*l.^2+2*l-1)./(l.*(l+1).*(l+2).*(l-1));    %generate array of Z
factors
ul=R^2*KT./(k.*(l+2).*(l-1).*(l.*(l+1)+s*R^2/k));       %generate array of u
factors
wl=(k*(l.*(l+1)+s*R^2/k))./(eta*R^3.*Z);                %generate array of w
factors
clear w                                          %the above factors reference
equations provides in Betz and Sykes

for n=1:length(f)
    w(n)=f(n)*2*pi;    %convert frequency to rad/s
        S_l=2.*ul.*wl./((wl.^2+w(n)^2)).*(2*l+1)/(4*pi);    %generate array
of PSD values at each mode for a certain frequency
    S(n)=sum(S_l);  %sum PSD values into one value per frequency

end
f=w/(2*pi); %regenerate frequency in Hz
```

BIBLIOGRAPHY

1. Muddana, H. S., Gullapalli, R. R., Manias, E. & Butler, P. J. Atomistic simulation of lipid and DiI dynamics in membrane bilayers under tension. *Phys. Chem. Chem. Phys.* **13,** 1368–78 (2011).
2. Langmuir, I. The mechanism of the surface phenomena of flotation. *Trans. Faraday Soc.* **15,** 62–74 (1920).
3. Sun, W. J. *et al.* Order and disorder in fully hydrated unoriented bilayers of gel phase dipalmitoylphosphatidycholine. *Phys. Rev. E* **49,** 4665–4676 (1994).
4. Kucerka, N., Kiselev, M. a & Balgavý, P. Determination of bilayer thickness and lipid surface area in unilamellar dimyristoylphosphatidylcholine vesicles from small-angle neutron scattering curves: a comparison of evaluation methods. *Eur. Biophys. J.* **33,** 328–334 (2004).
5. Seto, H., Yamada, N. L., Nagao, M., Hishida, M. & Takeda, T. Bending modulus of lipid bilayers in a liquid-crystalline phase including an anomalous swelling regime estimated by neutron spin echo experiments. *Eur. Phys. J. E* **26,** 217–223 (2008).
6. Nagle, J. F., Jablin, M. S., Tristram-nagle, S. & Akabori, K. What are the true values of the bending modulus of simple lipid bilayers ? *Chem. Phys. Lipids* **185,** 3–10 (2015).
7. Guo, Y., Pogodin, S. & Baulin, V. A. General model of phospholipid bilayers in fluid phase within the single chain mean field theory. *J. Chem. Phys.* **140,** (2014).
8. Betz, T. & Sykes, C. Time resolved membrane fluctuation spectroscopy. *Soft Matter* **8,** 5317 (2012).
9. Betz, T., Lenz, M., Joanny, J.-F. & Sykes, C. ATP-dependent mechanics of red blood

cells. *Proc. Natl. Acad. Sci. U. S. A.* **106,** 15320–15325 (2009).

10. Valeur, B. *Molecular Fluorescence: Principles and Applications*. **8,** (Wiley-VCH, 2002).
11. Gullapalli, R. R., Tabouillot, T., Mathura, R., Dangaria, J. H. & Butler, P. J. Integrated multimodal microscopy, time-resolved fluorescence, and optical-trap rheometry: toward single molecule mechanobiology. *J. Biomed. Opt.* **12,** 014012 (2007).
12. Becker, W. *The bh TCSPC Handbook*. (Becker & Hickl GmbH, 2006).
13. Kinoshita, S., Ohta, H. & Kushida, T. Subnanosecond fluorescence-lifetime measuring system using single photon counting method with mode-locked laser excitation. *Rev. Sci. Instrum.* **52,** 572 (1981).
14. Elson, E. L. & Magde, D. Fluorescence correlation spectroscopy. I. Conceptual basis and theory. *Biopolymers* **13,** 1–27 (1974).
15. Magde, D., Elson, E. L. & Webb, W. W. Fluorescence Correlation. II. An Experimental Realization. *Biopolymers* **13,** 29–61 (1974).
16. Krichevsky, O. & Bonnet, G. Fluorescence correlation spectroscopy: the technique and its applications. *Reports Prog. Phys.* **65,** 251–97 (2002).
17. Hess, S. T., Huang, S., Heikal, A. A. & Webb, W. W. Biological and Chemical Applications of Fluorescence Correlation Spectroscopy: A Review. *Biochemistry* **41,** 697–705 (2002).
18. Lakowicz, J. R. *Principles of Fluorescence Spectroscopy*. (Springer Science+Business Media, 2006).
19. Widengren, J., Mets, U. & Rigler, R. Fluorescence correlation spectroscopy of triplet states in solution: a theoretical and experimental study. *J. Phys. Chem.* **99,** 13368–13379 (1995).

20. Wachsmuth, M., Waldeck, W. & Langowski, J. Anomalous diffusion of fluorescent probes inside living cell nuclei investigated by spatially-resolved fluorescence correlation spectroscopy. *J. Mol. Biol.* **298,** 677–89 (2000).

21. Lampert, R. a. *et al.* Standards for nanosecond fluorescence decay time measurements. *Anal. Chem.* **55,** 68–73 (1983).

22. Lakowicz, J. R., Laczko, G., Cherek, H., Gratton, E. & Limkeman, M. Analysis of fluorescence decay kinetics from variable-frequency phase shift and modulation data. *Biophys. J.* **46,** 463–77 (1984).

23. Dowling, K. *et al.* Fluorescence lifetime imaging with picosecond resolution for biomedical applications. *Opt. Lett.* **23,** 810–812 (1998).

24. Grinvald, A. & Steinberg, I. Z. On the analysis of fluorescence decay kinetics by the method of least-squares. *Anal. Biochem.* **59,** 583–598 (1974).

25. Isenberg, I. & Dyson, R. D. The analysis of fluorescence decay by a method of moments. *Biophys J* **9,** 1337–1350 (1969).

26. Muddana, H. S., Morgan, T. T., Adair, J. H. & Butler, P. J. Photophysics of Cy3-Encapsulated Calcium Phosphate Nanoparticles. *Nano Lett.* **9,** 1559–1566 (2010).

27. Magde, D., Rojas, G. E. & Seybold, P. G. Solvent Dependence of the Fluorescence Lifetimes of Xanthene Dyes. *Photochem. Photobiol.* **70,** 737 (1999).

28. Neuman, K. C. & Block, S. M. Optical trapping. *Rev. Sci. Instrum.* **75,** 2787–2809 (2004).

29. Edidin, M. Lipids on the frontier: a century of cell-membrane bilayers. *Nat. Rev. Mol. Cell Biol.* **4,** 414–418 (2003).

30. Jacobson, K., Mouritsen, O. G. & Anderson, R. G. W. Lipid rafts: at a crossroad between cell biology and physics. *Nat. Cell Biol.* **9,** 7–14 (2007).

31. Simons, K. & Toomre, D. Lipid rafts and signal transduction. *Nat. Rev. Mol. Cell Biol.* **1,** 31–39 (2000).

32. Alberts, B. *et al.* in *Essential Cell Biology* (eds. Jeffcock, E. & Masson, S.) 364–372 (Garland Science, Taylor & Francis Group, 2010).

33. Nans, A., Mohandas, N. & Stokes, D. L. Native ultrastructure of the red cell cytoskeleton by cryo-electron tomography. *Biophys. J.* **101,** 2341–2350 (2011).

34. Strey, H., Peterson, M. & Sackmann, E. Measurement of erythrocyte membrane elasticity by flicker eigenmode decomposition. *Biophys. J.* **69,** 478–488 (1995).

35. Campillo, C. *et al.* Unexpected membrane dynamics unveiled by membrane nanotube extrusion. *Biophys. J.* **104,** 1248–1256 (2013).

36. Bao, G. & Suresh, S. Cell and molecular mechanics of biological materials. *Nat. Mater.* **2,** 715–725 (2003).

37. Huang, H., Kamm, R. D. & Lee, R. T. Cell mechanics and mechanotransduction : pathways , probes , and physiology. *Am. J. Physiol. Cell Physiol.* **287,** C1–C11 (2004).

38. Janmey, P. A. & McCulloch, C. A. Cell Mechanics: Integrating Cell Responses to Mechanical Stimuli. *Annu. Rev. Biomed. Eng.* **9,** 1–34 (2007).

39. Kung, C. A possible unifying principle for mechanosensation. *Nature* **436,** 647–654 (2005).

40. Huang, C. *et al.* Substrate Stiffness Regulates Cellular Uptake of Nanoparticles. *Nano Lett.* **13,** 1611–1615 (2013).

41. Jaalouk, D. E. & Lammerding, J. Mechanotransduction gone awry. *Nat. Rev. Mol. Cell. Biol.* **10,** 63–73 (2009).

42. Kandasamy, S. K. & Larson, R. G. Molecular dynamics simulations of model trans-

membrane peptides in lipid bilayers: a systematic investigation of hydrophobic mismatch. *Biophys. J.* **90,** 2326–2343 (2006).

43. Sang, H. P. & Opella, S. J. Tilt angle of a trans-membrane helix is determined by hydrophobic mismatch. *J. Mol. Biol.* **350,** 310–318 (2005).

44. Butler, P., Muddana, H. & Farag, S. in *Cell and Matrix Mechanics* (eds. Kaunas, R. & Zemel, A.) 35–62 (CRC Press, 2014).

45. Axelrod, D. Lateral motion of membrane proteins and biological function. *J. Membr. Biol.* **75,** 1–10 (1983).

46. Butler, P. J., Norwich, G., Weinbaum, S. & Chien, S. H. U. Shear stress induces a time- and position-dependent increase in endothelial cell membrane fluidity. *Am. J. Physiol. Cell Physiol.* **280,** 962–969 (2001).

47. Butler, P. J., Tsou, T. C., Li, J. Y. S., Usami, S. & Chien, S. Rate sensitivity of shear-induced changes in the lateral diffusion of endothelial cell membrane lipids: a role for membrane perturbation in shear-induced MAPK activation. *FASEB J.* **16,** 216–218 (2002).

48. García-Sáez, A. J., Chiantia, S. & Schwille, P. Effect of line tension on the lateral organization of lipid membranes. *J. Biol. Chem.* **282,** 33537–33544 (2007).

49. Heinrich, M., Tian, A., Esposito, C. & Baumgart, T. Dynamic sorting of lipids and proteins in membrane tubes with a moving phase boundary. *Proc. Natl. Acad. Sci. U. S. A.* **107,** 7208–7213 (2010).

50. Lepzelter, D. & Zaman, M. H. Clustered diffusion of integrins. *Biophys. J.* **99,** L106–L108 (2010).

51. Helfrich, W. Elastic Properties of Lipid Bilayers: Theory and Possible Experiments.

Zeitschrift fur Naturforsch. - Sect. C J. Biosci. **28,** 693–703 (1973).

52. Campelo, F., Arnarez, C., Marrink, S. J. & Kozlov, M. M. Helfrich model of membrane bending: From Gibbs theory of liquid interfaces to membranes as thick anisotropic elastic layers. *Adv. Colloid Interface Sci.* **208,** 25–33 (2014).

53. Marcelja, S. Chain Ordering in Liquid Crystals II. Structure of Bilayer Membranes. *Biochim. Biophys. Acta* **367,** 165–176 (1974).

54. Ou-Yang, Z. C. & Tu, Z. C. Overview of the Study of Complex Shapes of Fluid Membranes, the Helfrich Model and New Applications. *Int. J. Mod. Phys. B* **28,** 1330022 (2014).

55. Nelson, D. R., Piran, T. & Weinberg, S. in *Statistical Mechanics of Membranes and Surfaces* 64–66 (World Scientific, 2004).

56. Deserno, M. *Fluid lipid membranes – a primer*.

57. Evans, E. A. New membrane concept applied to the analysis of fluid shear and micropipette deformed red blood cells. *Biophys. J.* **13,** 941–954 (1973).

58. Evans, E. & Weitz, D. A. Entropy-Driven Tension and Bending Elasticity in Condensed-Fluid Membranes. *Phys. Rev. Lett.* **64,** 2094–2097 (1990).

59. Olbrich, K., Rawicz, W., Needham, D. & Evans, E. Water permeability and mechanical strength of polyunsaturated lipid bilayers. *Biophys. J.* **79,** 321–7 (2000).

60. Evans, E. & Needham, D. Physical properties of surfactant bilayer membranes: thermal transitions, elasticity, rigidity, cohesion and colloidal interactions. *J. Phys. Chem.* **91,** 4219–4228 (1987).

61. Evans, E. A. Bending elastic modulus of red blood cell membrane derived from buckling instability in micropipet aspiration tests. *Biophys. J.* **43,** 27–30 (1983).

62. Liu, Y. F. & Nagle, J. Diffuse scattering provides material parameters and electron density profiles of biomembranes. *Phys. Rev. E* **69,** (2004).

63. Lyatskaya, Y., Liu, Y. F., Tristram-Nagle, S. T., Katsaras, J. & Nagle, J. F. Method for obtaining structure and interactions from oriented lipid bilayers. *Phys. Rev. E* **63,** (2001).

64. Méléard, P., Pott, T., Bouvrias, H. & Ipsen, J. H. Advantages of statistical analysis of giant vesicle flickering for bending elasticity measurements. *Eur. Phys. J. Soft Matter Biol. Phys.* **34,** 116–130 (2011).

65. Zilker, A., Engelhardt, H. & Sackmann, E. Dynamic reflection interference contrast (RIC-) microscopy : a new method to study surface excitations of cells and to measure membrane bending elastic moduli. *J. Phys.* **48,** 2139–2151 (1987).

66. Park, Y. *et al.* Measurement of red blood cell mechanics during morphological changes. *Proc. Natl. Acad. Sci. U. S. A.* **107,** 6731–6 (2010).

67. Popescu, G. *et al.* Optical measurement of cell membrane tension. *Phys. Rev. Lett.* **97,** 1–4 (2006).

68. Sun, W. J., Tristram-Nagle, S., Suter, R. M. & Nagle, J. F. Structure of gel phase saturated lecithin bilayers: temperature and chain length dependence. *Biophys. J.* **71,** 885–891 (1996).

69. Sun, W.-J. *et al.* Order and disorder in fully hydrated unoriented bilayers of gel-phase dipalmitoylphosphatidylcholine. *Phys. Rev. E* **49,** 4665–4676 (1994).

70. Boscia, A. L. *et al.* X-ray structure , thermodynamics , elastic properties and MD simulations of cardiolipin / dimyristoylphosphatidylcholine mixed membranes. *Chem. Phys. Lipids* **178,** 1–10 (2014).

71. Kucerka, N. *et al.* Lipid bilayer structure determined by the simultaneous analysis of

neutron and X-ray scattering data. *Biophys. J.* **95,** 2356–2367 (2008).

72. Balgavý, P. *et al.* Bilayer thickness and lipid interface area in unilamellar extruded 1,2-diacylphosphatidylcholine liposomes: a small-angle neutron scattering study. *Biochim. Biophys. Acta* **1512,** 40–52 (2001).

73. Kucerka, N. *et al.* Structure of fully hydrated fluid phase DMPC and DLPC lipid bilayers using X-ray scattering from oriented multilamellar arrays and from unilamellar vesicles. *Biophys. J.* **88,** 2626–2637 (2005).

74. Lenz, O. & Schmid, F. A simple computer model for liquid lipid bilayers. *J. Mol. Liq.* **117,** 147–152 (2005).

75. Uusitalo, J. J. *et al.* Dry Martini, a Coarse-Grained Force Field for Lipid Membrane Simulations with Implicit Solvent. *J. Chem. Theory Comput.* **11,** 260–275 (2015).

76. Chacón, E. *et al.* A computer simulation approach to quantify the true area and true area compressibility modulus of biological membranes. *J. Chem. Phys.* **143,** 1–11 (2015).

77. Khelashvili, G., Johner, N., Zhao, G., Harries, D. & Scott, H. L. Molecular origins of bending rigidity in lipids with isolated and conjugated double bonds : The effect of cholesterol. *Chem. Phys. Lipids* **178,** 18–26 (2014).

78. Levine, Z. A. *et al.* Determination of Biomembrane Bending Moduli in Fully Atomistic Simulations. *J. Am. Chem. Soc.* **136,** 13582–13585 (2014).

79. Pogodin, S. & Baulin, V. A. Coarse-grained models of phospholipid membranes within the single chain mean field theory. *Soft Matter* **6,** 2216–2226 (2010).

80. Guo, Y. *et al.* General model of phospholipid bilayers in fluid phase within the single chain mean field theory. *J. Chem. Phys.* **140,** 1–9 (2014).

81. Loufty, R. O. & Arnold, B. A. Effect of Viscosity and Temperature on Torsional

Relaxation of Molecular Rotors. *J. Phys. Chem.* **86,** 4205–4211 (1982).

82. Brochard, F. & Lennon, J. F. Frequency spectrum of the flicker phenomenon in erythrocytes. *J. Phys.* **36,** 1035–1047 (1975).

83. Seifert, U. Configurations of fluid membranes and vesicles. *Adv. Phys.* **46,** 13–137 (1997).

84. Lingwood, D. & Simons, K. Lipid rafts as a membrane-organizing principle. *Science* **327,** 46–50 (2010).

85. Tabouillot, T., Muddana, H. S. & Butler, P. J. Endothelial Cell Membrane Sensitivity to Shear Stress is Lipid Domain Dependent. *Cell. Mol. Bioeng.* **4,** 169–181 (2011).

86. Engelman, D. M. Surface area per lipid molecule in the intact membrane of the human red cell. *Nature* **223,** 1279–1280 (1969).

87. Gov, N., Zilman, a G. & Safran, S. Cytoskeleton Confinement and Tension of Red Blood Cell Membranes. *Phys. Rev. Lett.* **90,** 228101 (2003).

88. Gov, N. S. & Safran, S. A. Red Blood Cell Membrane Fluctuations and Shape Controlled by ATP-Induced Cytoskeletal Defects. *Biophys. J.* **88,** 1859–1874 (2005).

89. Spector, A. A., John, K. & Fletcher, J. E. Binding of long-chain fatty acids to bovine serum albumin. *J. Lipid Res.* **10,** 56–67 (1969).

90. Goto, K. & Mizushima, S. Removal by bovine serum albumin of fatty acids from membrane vesicles and its effect on proline transport activity in Escherichia coli. *J. Biochem.* **84,** 251–258 (1978).

91. Khairy, K., Foo, J. & Howard, J. Shapes of Red Blood Cells: Comparison of 3D Confocal Images with the Bilayer-Couple Model. *Cell. Mol. Bioeng.* **1,** 173–181 (2008).

92. Mastro, A. M., Babich, M. A., Taylor, W. D. & Keith, A. D. Diffusion of a small molecule in the cytoplasm of mammalian cells (cytoplasmic viscosity/electron spin

resonance/cytoskeleton/fibroblasts). *Proc. Natl. Acad. Sci.* **81,** 3414–3418 (1984).

93. Yoon, Y. Z. *et al.* Flickering analysis of erythrocyte mechanical properties: Dependence on oxygenation level, cell shape, and hydration level. *Biophys. J.* **97,** 1606–1615 (2009).

ACADEMIC VITA

Academic Vita of Nicholas Frazzette
nfrazzette@gmail.com

Education

Pennsylvania State University, Schreyer Honors College and College of Engineering

University Park, PA. Combined BS/MS in Bioengineering, 2016, minoring in Spanish

Work, Research, and Teaching Experience

Peter J. Butler Mechanical-bioengineering Lab

02/2012-present

Used time-correlated single photon counting microscopy to (1) analyze calcium-phosphate or lipid membrane nanocarriers as vehicles for intracellular bioimaging dyes and delivery systems for siRNA-based chemotherapeutics, (2) characterize enhanced enzyme diffusivity observed in catalysis by observing changes in local solution viscosity and temperature, and (3) develop a novel method for measuring membrane bending fluidity by observing changes in membrane-integrated fluorophores

Biomedical Engineering Department

08/2014-present

Developed a graduate-level, experiment based laboratory course, with emphasis on additive manufacturing, biomaterial development and analysis, and hemaflow analysis, for an accelerated Master's in Bioengineering program; collaborated with BME and other engineering faculty

Redesigned and helped instruct BME 100S: Biomedical Engineering Seminar, the introductory first-year seminar for students interested in the biomedical engineering major as part of the College of Engineering Teaching Intern program

Graded assignments for BME 402: Biomedical Instrumentation and Measurement

Humanitarian Engineering and Social Entrepreneurship Program

01/2015-present

Designed and evaluated (1) novel urinalysis test strip produced via repurposed inkjet printing for resourced-constrained contexts, and (2) venture-model for commercializing test strip and empowering vendors/community health workers;

Selected to attend the 2015 Global Grand Challenges Summit in Beijing, China hosted by the Chinese Academy of Engineering with the US National Academy of Engineering and British Royal Academy of Engineering;

Edited scholarly papers for submission to peer-reviewed journals focusing on entrepreneurship, engineering, and innovation

Summer Translational Cardiovascular Sciences Institute

06/2013-08/2013

Awarded a grant funded by the AHA to determine the effects of shear stress on nanoliposomal membranes for increased permeability to siRNA as a potential drug delivery system for genetic and other intracellular cardiomyopathies

Leadership

Penn State Engaged Scholarship Initiative

02/2015-present

Worked with Penn State Student Affairs administration to develop opportunities and strategies and craft presentations to increase student involvement in outside-the-classroom learning experiences, such as Study Abroad, Undergraduate Research, and Internships; served as an Engaged Scholarship Student Ambassador providing mentorship to interested underclassmen

Grand Global Challenge Scholar Program

07/2015-present

Collaborated with faculty in the College of Engineering to develop a certificate program for engineering design focused on global challenges set forth by the United Nations and US National Academy of Engineering; program includes a research project which generates meaningful impact and includes student reflection

Springfield, Benefiting THON

10/2011-present

Served on leadership positions (Donor Relations, Community) to develop a fundraising student-organization working with the Four Diamonds, a pediatric cancer nonprofit; as Donor Relations, solicited corporate donors and saw a 34% increase in fundraising; as Community, led a team of 12 social captains and planned major social events

Leonhard Center for Enhancement of Engineering Education

09/2011-present

Awarded a yearly scholarship for academic performance; assisted College of Engineering in developing future goals, mission statements, "World-class Engineer" graduation standard

Schreyer Honors College Day of Service

09/2012-10/2013

Served on leadership positions (Sponsorship, Service Site Coordinator) to organize and execute a daylong volunteer and service effort for students in the Honors College; as Sponsorship, solicited businesses for monetary or in-kind; as Service Site Coordinator, contacted local charitable ventures and organized transportation to and from service sites for volunteers

Leadership Jumpstart Program

02/2012-11/2015

Redesigned and helped instruct EDTHP 234H: Leadership Jumpstart, a first year, honors-level course providing experiential introduction to and radical development of leadership skills such as personal assessments, team building, collaboration, civics and ethics, and policy generation, and EDTHP 434H: Teaching Experience in Leadership Jumpstart

LeaderShape Institute

05/2012

Participant – spent one week on retreat surveying different styles and methods of leadership, personality analyses, and case studies – learned formal and informal communication skills, leadership lessons, stress management skills

Skills, Awards, and Achievements

Skills

- Intermediate proficiency in Spanish language (reading, writing, conversation)
- Basic proficiency in CAD software, COMSOL, statistical software; high proficiency in MATLAB

Awards

- NSF Summer Research Grant: Summer 4
- Summer Discovery Research Grant: Summer 3
- College of Engineering Research Experience for Undergraduates Grant: Summer 3
- STCSI Summer Research Grant: Summer 2
- Schreyer Honors College Academic Excellence Scholarship: Semesters 1-8
- College of Engineering Leonhard Program International Travel Grant: Summer 4
- Leonhard Honors Program Scholarship: Semesters: 1-8
- Morrow End Scholarship and Jones Scholarship College of Engineering: Semesters 1-8
- John W. White Scholarship for Excellence in Spanish: Semesters 5, 6
- Student Leadership Scholarship: Semesters 4, 6

Achievements

- Student Marshal for Biomedical Engineering, Spring Commencement 2016
- Grand Challenge Scholar
- Dean's List: Semesters: 1-8, Summer 1

Publications

Nicholas Frazzette, Jennifer Dobson, Arwa Mukhtar, Bridget Burt, Janak Jethva, James H. Adair, Khanjan Mehta. "Can We Manufacture Diagnostic Test Strips Using an Inkjet Printer?" *IEEE 2015 Global Humanitarian Technology Conference*. pp. 431-436. (2015).

Nicholas Frazzette, Janak Jethva, Khanjan Mehta, Josh Stapleton, Clive Randall. “Designing a Ruggedization Lab to Characterize Materials for Harsh Environment:. *Journal of Medical Engineering & Technology*. (2016) (in review)

Kathryn Ortbal, Nicholas Frazzette, Khanjan Mehta. “Stakeholder-Personas: An Educational Tool for Social Entrepreneurs”. *Humanitarian Technology: Science, Systems, and Global Impact 2016*. (2016). (in review)

Kathryn Ortbal, Nicholas Frazzette, Khanjan Mehta. “Stakeholder Journey Mapping: A Business Development Tool for Social Entrepreneurs”. *Humanitarian Technology: Science, Systems, and Global Impact 2016*. (2016). (in review)